TRIMS LST: A daily 1-km all-weather land surface temperature dataset for the Chinese landmass and surrounding areas (2000–2022)

Wenbin Tang[1], Ji Zhou[1], Jin Ma[1], Ziwei Wang[1], Lirong Ding[1], Xiaodong Zhang[2, 3], Xu Zhang[1]

[1] School of Resources and Environment, University of Electronic Science and Technology of China, Chengdu 611731, China

[2] Shanghai Aerospace Electronic Technology Institute, Shanghai 201109, China

[3] Shanghai Spaceflight Institute of TT&C and Telecommunication, Shanghai 201109, China

Correspondence to: Ji Zhou (jzhou233@uestc.edu.cn)

Abstract. Land surface temperature (LST) is a key variable within the Earth's climate system and a necessary input parameter required by numerous land-atmosphere models. It can be directly retrieved from satellite thermal infrared (TIR) observations, but cloud contamination results in many invalid pixels. To investigate the temporal and spatial variations of LST in China, long-term, high-quality, and spatio-temporally continuous LST datasets (i.e., all-weather LST) are urgently needed. Fusing satellite TIR LST and reanalysis datasets is a viable route to obtain long time-series all-weather LST. Among satellite TIR LSTs, the MODIS LST is the most commonly used and a few all-weather LST products generated in this way have been reported recently. However, the publicly reported all-weather LSTs are not available during the temporal gaps of MODIS between 2000 and 2002. In this context, we report a daily (four observations per day) 1-km all-weather LST dataset for the Chinese landmass and surrounding areas – TRIMS LST. Different from other products, the TRIMS LST begins on the first day of the new millennium (i.e., January 1, 2000). The TRIMS LST was generated based on the Enhanced Reanalysis and Thermal infrared remote sensing Merging (E-RTM) method. Specifically, the original RTM method was used to generate the TRIMS LST outside the temporal gaps. Two newly developed approaches, including the Random-Forest based Spatio-Temporal Merging (RFSTM) approach and Time-SEquential LST based Reconstruction (TSETR) approach, were used to produce Terra/MODIS-based and Aqua/MODIS-based TRIMS LSTs during the temporal gaps, respectively. Thorough evaluation of the TRIMS LST was conducted. A comparison with the GLDAS and ERA5-Land LST demonstrates that TRIMS LST has similar spatial patterns but higher image quality, more spatial details, and no evident spatial discontinuities. The results outside the temporal gap show consistent comparisons of TRIMS LST with MODIS and/AATSR LST, with mean bias deviation (MBD) of 0.09 K/0.37 K and standard deviation of bias (STD) of 1.45 K/1.55 K. Validation based on *in-situ* LST at 19 ground sites indicate that the TRIMS LST has a mean bias error (MBE) ranging from -2.26 K to 1.73 K and a root mean square error (RMSE) ranging from 0.80 K to 3.68 K. There is no significant difference between the clear-sky and cloudy conditions. For the temporal gap, it is observed that RFSTM and TSETR perform similarly to the original RTM method. Additionally, the differences between Aqua and Terra remain stable throughout the temporal gap. The TRIMS LST has already been used by scientific communities in various applications such as soil moisture downscaling, evapotranspiration estimation,

and urban heat island modelling. The TRIMS LST is freely and conveniently available at https://doi.org/10.11888/Meteoro.tpdc.271252 (Zhou et al., 2021).

1 Introduction

Land surface temperature (LST) is a key variable related to the energy exchange at the interface between the land surface and the atmosphere. It is the result of the thermal feedback of various ground surface to incident solar radiation and atmospheric downward radiation. Therefore, it is a necessary input parameter required by numerous land–atmosphere models (Jiang and Liu, 2014; Li et al., 2013b, 2023c). LST have been widely used in a variety of studies, such as surface evapotranspiration (ET) estimation (Anderson et al., 2011; Ma et al., 2022), urban heat island (UHI) modelling (Alexander, 2020; Liao et al., 2022), drought monitoring (Zhang et al., 2017), and ecological assessment (Sims et al., 2008).

In the past four decades, especially since the beginning of the new millennium (i.e., 2000), China and its surrounding areas have experienced rapid economic development and population growth, accompanied by notable changes to the natural environment (Yang and Huang, 2021). Meanwhile, China has adopted a series of interventions to protect the environment since the 1980s, such as the Grain for Green Program (Wang et al., 2017), Three-North Shelter Forest Program (Zhai et al., 2023), and Red Lines of Cropland (a policy to ensure that Chinese arable land does not drop below 120 million hectares). These interventions have played a key role in changing the land use/cover and regulating the climate (Chen et al., 2019a). In addition, with the warming climate, extreme weather and meteorological disasters occur frequently in China and its surrounding areas (Chen et al., 2019b). Since LST is highly sensitive to land cover change, heat waves, droughts, and vegetation information (Li et al., 2023a; Su et al., 2023), making it an important indicator of global climate change (Mildrexler et al., 2018; Peng et al., 2014), it is important to investigate the spatial and temporal variations of LST for these areas. This requires a long-term, high-quality, and spatio-temporally continuous LST dataset.

LST can be obtained through *in-situ* observations, model simulations, and remote sensing retrievals. However, LST is spatially and temporally heterogeneous and highly affected by various factors such as land cover, soil type, topography, climatic, and meteorological conditions (Liu et al., 2006; Zhan et al., 2013). *In-situ* observations based on spatial 'point measurement' are not able to obtain spatially continuous LST, and the current model simulation suffer from coarse spatial resolution. In contrast, satellite remote sensing, which has advantages of better spatial continuity, larger coverage, good ability for repeating observations, and much higher spatial resolution, has become an important way to obtain LST for large areas (Li et al., 2013b). Satellite thermal infrared (TIR) remote sensing can directly obtain the regional and global LST efficiently. A series of satellite TIR LST products are currently available to users, including platforms such as polar orbiting and geostationary satellite platforms. Among the satellite TIR LST products, the Moderate-resolution Imaging Spectroradiometer (MODIS) LST products is the most widely used because of its global coverage, long time-series (since February 24, 2000 for Terra and since July 4, 2002 for Aqua), high quality, and good accuracy (Aguilar-Lome et al., 2019; Sandeep et al., 2021; Wan, 2014).

Although MODIS LST products (especially with a 1-km spatial resolution) have shown good performance in related applications, they generally have significant spatial absences due to cloud contamination, especially in low and middle latitudes in China (e.g., the Tibet Plateau and southern China) (Duan et al., 2017). Cloud contamination restricts the LST products from playing a more critical role in subsequent applications (Li et al., 2023c). Furthermore, there is a temporal discontinuity (hereafter termed as the temporal gap) in Terra/Aqua MODIS during 2000-2002; thus, it is not easy to generate the all-weather LST products for these gaps.

In recent years, many methods have been developed to generate all-weather LST based on satellite TIR LST and other data (Jia et al., 2022; Zhang et al., 2022). Typical methods include spatial-temporal interpolation, surface energy balance (SEB), and multisource data integration (Ding et al., 2023; Li et al., 2023c). The spatial-temporal interpolation methods take advantage of temporal variation patterns of the LST as well as the spatial characteristics. One of the most representative study come from Zhang et al. (2022), which takes full advantage of above patterns and characteristics in their spatiotemporal fitting framework to generate a 1-km spatial resolution dataset from 2003 to 2020 over global land. According to our knowledge, this dataset is the first seamless daily 1-km resolution LST dataset with global spatial coverage and the only seamless one on Google Earth Engine for free applications. Nevertheless, it is crucial to acknowledge that the results obtained by the above methods are the hypothetical LST under clear-sky conditions, not the LST in the cloud-contaminated regions (Martins et al., 2019). To solve the above problems, SEB is proposed as a physical method (Jin and Dickinson, 2000). Under cloudy conditions, this method considers longwave radiation and solar radiation as influences on the LST. Martins et al. (2019) used the SEB method to successfully fill the missing LST using land surface parameters provided by the European Satellite Application Facility on Land Surface Analysis (LSA-SAF) and generate the all-weather LST product (MSG All-Sky Land Surface Temperature, MLST-AS). In addition, a more general approach that incorporates the clear-sky LST into the SEB has recently been developed to estimate the LSTs under cloud-contaminated regions based on the MODIS and Visible infrared Imaging Radiometer (VIIRS) data (Jia et al., 2021).

At present, multisource data integration methods have been widely used to generate seamless all-weather LST. Present multisource data fusion methods mainly to integrate TIR LST with satellite passive microwave (PMW) observation or reanalysis data. PMW data can be used for estimating all-weather LST retrievals because they are less affected by the atmosphere and clouds (Holmes et al., 2009; Zhou et al., 2017). However, there are limitations in obtaining all-weather LST from PMW observations. First, the spatial resolution of PMW data differs significantly from TIR, such as the Advanced Microwave Scanning Radiometer 2 (AMSR2) with ~10 km spatial resolution. Second, the spatial coverage of the PMW data is incomplete because there are orbital gaps. Third, the temperature retrieved from PMW observations contains information from the subsurface, which differs from the TIR LST that exclusively represents skin temperature (Zhou et al., 2017). Compared with the PMW data, reanalysis data can provide spatially continuous LST and related surface parameters; thus, it can act as an alternative basis to obtain the all-weather LST (Long et al., 2020; Ding et al., 2022). One typical method is the Reanalysis and Thermal infrared remote sensing Merging (RTM) method proposed by Zhang et al. (2021) for integrating the GLDAS and MODIS LST for the Tibetan Plateau.

98   In recent years, based on the aforementioned three typical methods, various all-weather LST datasets were released (Duan et

99   al., 2017; Hong et al., 2022; Jia et al., 2022; Li et al., 2021a; Metz et al., 2017; Muñoz-Sabater et al., 2021; Yao et al., 2023;

100   Yu et al., 2022). However, all-weather LST datasets with both high temporal resolution (4 observations per day or higher) and

101   high spatial resolution (1 km or higher) since 2000 for the Chinese landmass and the surrounding areas are still rare.

102   In this study, we proposed the enhanced RTM (E-RTM) method to produce a daily (four observations per day) 1-km all-

103   weather LST dataset for the Chinese landmass and surrounding areas (19°N–55°N, 72°E–135°E), which is known as the

104   Thermal and Reanalysis Integrating Moderate-resolution Spatial- seamless LST (TRIMS LST). The E-RTM method includes

105   three modules (Sect.3). The original RTM method is used to produce the TRIMS LST during DOY 55 of 2000 (DOY 185 of

106   2002) to DOY365 of 2022. Additionally, based on the physical properties of the LST time component decomposition model,

107   Terra/MODIS-based and Aqua/MODIS-based TRIMS LST during the temporal gaps are produced. Then TRIMS LST is

108   evaluated using *in-situ* sites to provide better-quality data for applications associated with urban thermal environment,

109   meteorology, and hydrology.

110   **2 Datasets**

111   **2.1 Satellite data and reanalysis data**

112   In this study, the main satellite data used are the 1-km daily MODIS LST/emissivity product (MOD11A1: February 2000 to

113   December 2022; MYD11A1: July 2002 to December 2022) in version 6.1. This LST product was produced based on the

114   generalized split-window algorithm and has good accuracy for homogeneous surfaces (Wan, 2014). As mentioned previously,

115   it is usually used as the basis in the reconstruction of all-weather LST. In this study, this product is also used as a basis data

116   for producing the TRIMS LST. The other used MODIS datasets used include: (1) the 1-km 16-day Normalized Difference

117   Vegetation Index (NDVI) product (MOD13A2: February 2000 to December 2022) in version 6.1; (2) the 500-m daily

118   Normalized Difference Snow Index (NDSI) product (MOD10A1F: February 2000 to December 2022) in version 6.1

119   (https://modis-snow-ice.gsfc.nasa.gov/); and (3) the 500-m daily MODIS land surface albedo product (MCD43A3: February

120   2000 to December 2022) in version 6.1. All of the above products except MOD10A1F are available at EARTHDATA

121   (https://earthdata.nasa.gov/). In addition to generation and evaluation of the all-weather LST, we also collected (1) the 90-m

122   Shuttle Radar Topography Mission Digital Elevation Model data (SRTM DEM; http://srtm.csi.cgiar.org); (2) Global 1-km

123   daily Synthesis of 'Satellite Pour l'Observation de la Terre' (SPOT) VEGETATION (VGT) Images (VGT-S1) (January 2000

124   to February 2000) (https://services.terrascope.be/) (Toté et al., 2017); (3) 0.05° 8-day GLASS Albedo product (January 2000

125   to February 2000) (http://www.glass.umd.edu/Albedo/MIX/) (Feng et al., 2016); (4) the 30-m yearly China land cover dataset

126   (2000-2015) from Zenodo (CLCD, https://doi.org/10.5281/zenodo.4417810) (Yang and Huang, 2021) and (5) the 1-km daily

127   ENVISAT/AATSR LST product (July 2004–April 2012) (https://climate.esa.int/).

128   The main reanalysis data used in this study are the Global Land Data Assimilation System assimilation (GLDAS) data

129   provided by the Goddard Earth Sciences Data and Information Services Center (GES DISC) (Rodell et al., 2004). GLDAS

130 utilizes an analysis increment, which is obtained through the optimal interpolator using the observed-minus-forecast value for

131 the skin temperature calculated by GLDAS. This analysis increment, along with the bias correction term, is subsequently

132 provided to the land surface models code for energy budget considerations. The bias correction ensures that the modelled state

133 is continually adjusted towards the observed values, thereby improving the accuracy of the skin temperature calculations on

134 an incremental, semi-daily, or daily basis (Radakovich et al., 2001). The accuracy of GLDAS LST has been demonstrated by

135 various studies with MBE ranging from -4.27 K to 8.65 K and RMSE ranging from 3.0 K to 6.02 K (Zhang et al.,2021; Xiao

136 et al.,2023). Specifically, the 0.25° 3-hourly LST from the GLDAS Noah model between January 2000 and December 2022

137 was used as another input of the RTM method. In addition, we also collected the 0.1° hourly ERA5-Land LST datasets (Muñoz-

138 Sabater et al., 2021), and its LST will be compared with the generated TRIMS LST.

2.2 Ground measurements

140 Table I shows 19 ground sites that recorded longwave radiation data for different time spans. According to geographical

141 locations and land cover types provided in Table I, it is clear that they are distributed in different climate zones. This indicates

142 that they encompass a wide range of land surface and climatic situations for sufficient validation of the TRIMS LST. The

143 measurement device at the selected ground station includes a long-wave radiometer and four-component radiometers,

144 including CNR1, CNR4, and CG4 (Kipp & Zonen, Netherlands; https://www.kippzonen.com/). According to the specifications

145 of these radiometers, the uncertainties in daily total for longwave radiation measurements are 3%–10% (Wang et al.,2020).

146 With the measured incoming and outgoing longwave radiation, the LST of the land cover type within the field-of-view (FOV)

147 of the radiometer can be calculated through the radiative transfer equation in the form of the Stephan-Boltzmann's law (Ma et

148 al., 2023, 2021). Considering the uncertainties of the longwave radiation measurement, the uncertainties of the calculated *in-*

149 *situ* LST are approximately 0.6 K–1.2 K (Xu et al., 2013; Yang et al., 2020; Ma et al., 2021).

150 Spatial representativeness of ground sites has different degrees of influence on the validation of TIR-based LST using *in-situ*

151 LST. In this study, to quantify the spatial representativeness, we calculated the standard deviation (STD) of 33 × 33 Landsat

152 LST within MODIS pixels containing ground sites. United States Geological Survey provides this product, which is the 30-m

153 Landsat-7 ETM+ Collection 2 Level-2 (L2C2) LST (U.S. Geological Survey, 2021). For the 19 sites, the STD was 0.64 K to

154 1.53 K, indicating good to acceptable representativeness of these sites for the validation of a 1-km LST (Zhang et al., 2021;

155 Duan et al., 2019). Abnormal measurements, caused by short-term disturbances such as instantaneous shadow from small

156 clouds and birds, were excluded from the ground measured longwave radiation through a quality check. This quality check

157 involved removing the outgoing or incoming longwave radiation that deviated by more than 3σ (standard deviations) from

158 their respective one-hour averages (Göttsche et al., 2016).
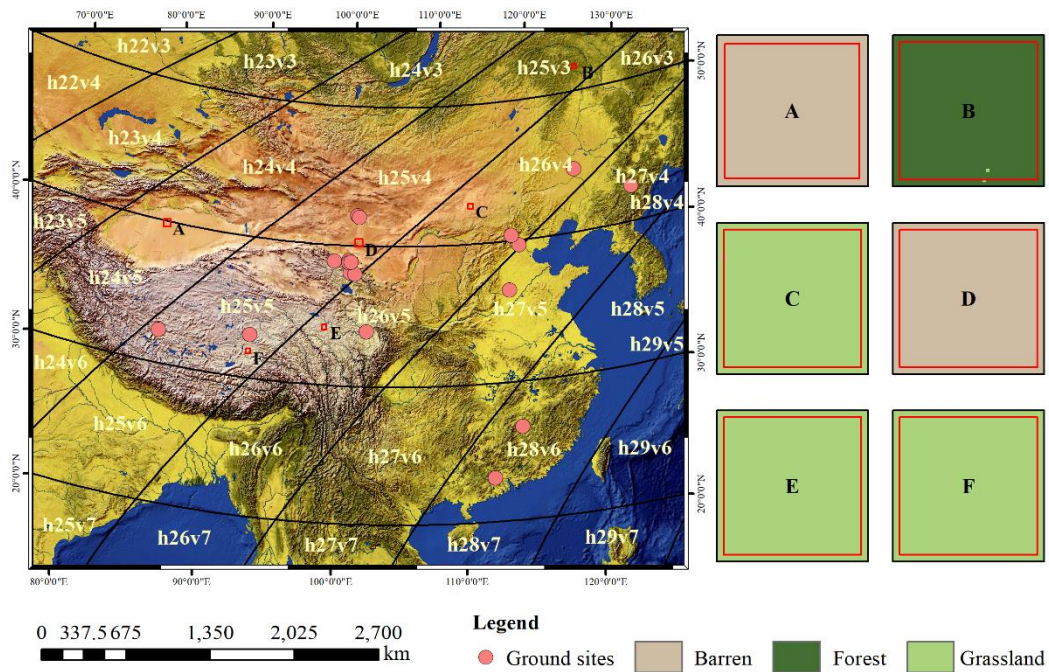
159
160 **Figure1: The study area and the selected 19 ground sites. A, B, C, D, E, and F are subareas exhibited a single land cover type with**
161 **no change in T1 and T2 (January 1 2000 to January 3 2005).**

162

Table I: Details of the 19 selected ground sites and their measurements.

Site	Latitude and Longitude (°N, °E)	Elevation (m)	Radiometers	Height of radiometer (m)	Diameter of radiometer's FOV (m)	Surface type	Period	STD of 30-m Landsat LST (K)	Source
Arou (ARO)	38.05, 100.46	3033	CNR4	5	37.32	Subalpine meadow	2013–2021	0.68	HiWATER
Daman (DAM)	38.86, 100.37	1556	CNR1	12	89.57	Cropland	2013–2021	0.78	HiWATER
Desert (DET)	42.11, 100.99	1054	CNR4	6	44.78	Desert	2015–2021	0.65	HiWATER
Dashalong (DSL)	38.84, 98.94	3739	CNR4	6	44.78	Marsh alpine meadow	2013–2021	1.29	HiWATER
Ebao (EBA)	37.95, 100.92	3294	CNR1	6	44.78	Alpine Meadow	2013–2016	1.00	HiWATER
Gobi (GOB)	38.92, 100.31	1562	CNR1	6	44.78	Gobi	2013–2015	1.01	HiWATER
Huazhaizi (HZZ)	38.77, 100.32	1735	CNR1	6	44.78	Desert	2013–2021	0.82	HiWATER
Sidaoqiao (SDQ)	42.00, 101.14	873	CNR1	10	74.64	Tamarix	2013–2021	1.53	HiWATER
Shenshawo (SSW)	38.79, 100.49	1555	CNR1	6	44.78	Desert	2014–2015	1.45	HiWATER
Huailai (HLA)	40.35, 115.79	480	CNR4	5	37.32	Cropland	2013–2020	1.32	HBE
D105	33.06, 91.95	5039	CNR1	1.34	10.00	Subalpine meadow	2002–2004	1.29	CEOP-CAMP
Gaize (GAZ)	32.31, 84.06	4416	CNR1	1.49	11.12	Barren land	2002–2004	1.48	CEOP-CAMP
Guantao (GUT)	36.52, 115.13	30	CNR1	15.7	117.19	Cropland	2009–2010	0.71	HBE
Changbaishan (CBS)	42.40, 128.10	736	CNR1	6*	44.78	Mixed forest	2006	1.33	China Flux
Daxing (DXI)	39.62, 116.43	20	CNR1	28	208.99	Cropland	2008-2010	1.46	HBE
Dinghushan (DHS)	23.17, 112.53	300	CNR1	19*	141.82	Broad-leaved evergreen forest	2006	0.67	CERN
Maqu (MQU)	33.89, 102.14	3423	CNR1	1.5	11.20	Grassland	2010	1.20	NIEER-CAS
Qianyanzhou (QYZ)	26.74, 115.06	75	CNR1	1.8	13.44	Evergreen coniferous forest	2010	1.42	CERN
Tongyu (TYU)	44.42, 122.87	184	CG4	3	22.39	Cropland	2003–2004	0.64	CEOP-CAMP

Note: *this height is the instrument's average height above the tree canopy. The ground sites were operated by different field campaigns or programs. CERN: Chinese Ecosystem Research Network (Fu et al., 2010; Pastorello et al., 2020); CEOP-CAMP: the Coordinated Energy and Water Cycle Observation Project (CEOP) and Asia-Australia Monsoon Project (CAMP) (Ma et al., 2006; Liu et al., 2004); China Flux (Pastorello et al., 2020; Yu et al., 2014; Zhang and Han, 2016); HBE: Haihe experiment (Guo et al., 2020; Liu et al., 2013b); HiWATER: Heihe Watershed Allied Telemetry Experimental Research (Che et al., 2019; Li et al., 2013a; Liu et al., 2011, 2018); NIEER-CAS: Northwest Institute of Eco-Environment and Resources, Chinese Academy of Sciences (Wen et al., 2011).

3. Methodology

TRIMS LST is generated through the E-RTM method, consisting of three modules depicted in Fig.2. Module I runs the original RTM method (Zhang et al., 2021) to merge MOD11A1 (MYD11A1) and GLDAS LST, producing daily all-weather LST at the Terra (Aqua) satellite overpass time from DOY 55 of 2000 (DOY 185 of 2002) to DOY 365 of 2022. Module II employs a Random-Forest based Spatio-Temporal Merging (RFSTM) approach to extend the beginning date of the MOD11A1 LST based all-weather LST to January 1, 2000. Finally, Module III utilizes a Time-SEquential LST based Reconstruction (TSETR) approach to extend the beginning date of the MYD11A1 LST based all-weather LST to January 1.

3.1 Module I: the RTM method

Details of the RTM method can be found in Zhang et al. (2021). For the convenience of readers, a brief description of RTM is provided here. In the temporal dimension, the time series of LST can be expressed as:

$$LST(t_{d}, t_{avg}, t_{ins}) = LFC(t_{d}, t_{avg}) + HFC(t_{d}, t_{avg}, t_{ins}) + HFC_{cld}(t_{d}, t_{ins}),\qquad(1)$$

where t_d is the day of year (DOY); t_{ins} is overpass time of a satellite TIR sensor (i.e., MODIS) and t_{avg} is the average observation time calculated from t_{ins}; LFC is the low frequency component that represents the intra-annual variation component of the LST under ideal clear-sky conditions; HFC is the high frequency component, which represents the sum of the diurnal LST variation and the weather variation component (WTC) under ideal clear-sky conditions; HFC_{cld} is a correction term representing the impact on LST triggered by cloud contamination under cloudy conditions; and HFC_{cld} is equal to zero under clear-sky conditions.

In the RTM method, LFC, HFC, and HFC_{cld} in Eq.(1) are first determined from the MODIS LST and the GLDAS LST. Then, the optimized models are determined for the three components according to their characteristics and their quality is improved by inputting their descriptors. Finally, three optimized components are integrated to generate the all-weather LST.

3.2 Module II: the RFSTM approach

The RFSTM approach was developed to predict the all-weather LST during the period of DOY 1-54 2000 during which the Terra/MODIS LST were not available. It is based on the fact that (i) the LST of a pixel in the temporal dimension is strongly affected by the meteorological conditions as well as the underlying surface and (ii) the LST of many pixels at a certain time are closely related to their underlying surfaces (Ma et al., 2021). Therefore, RFSTM has two stages, namely, the temporal stage and the spatial stage.
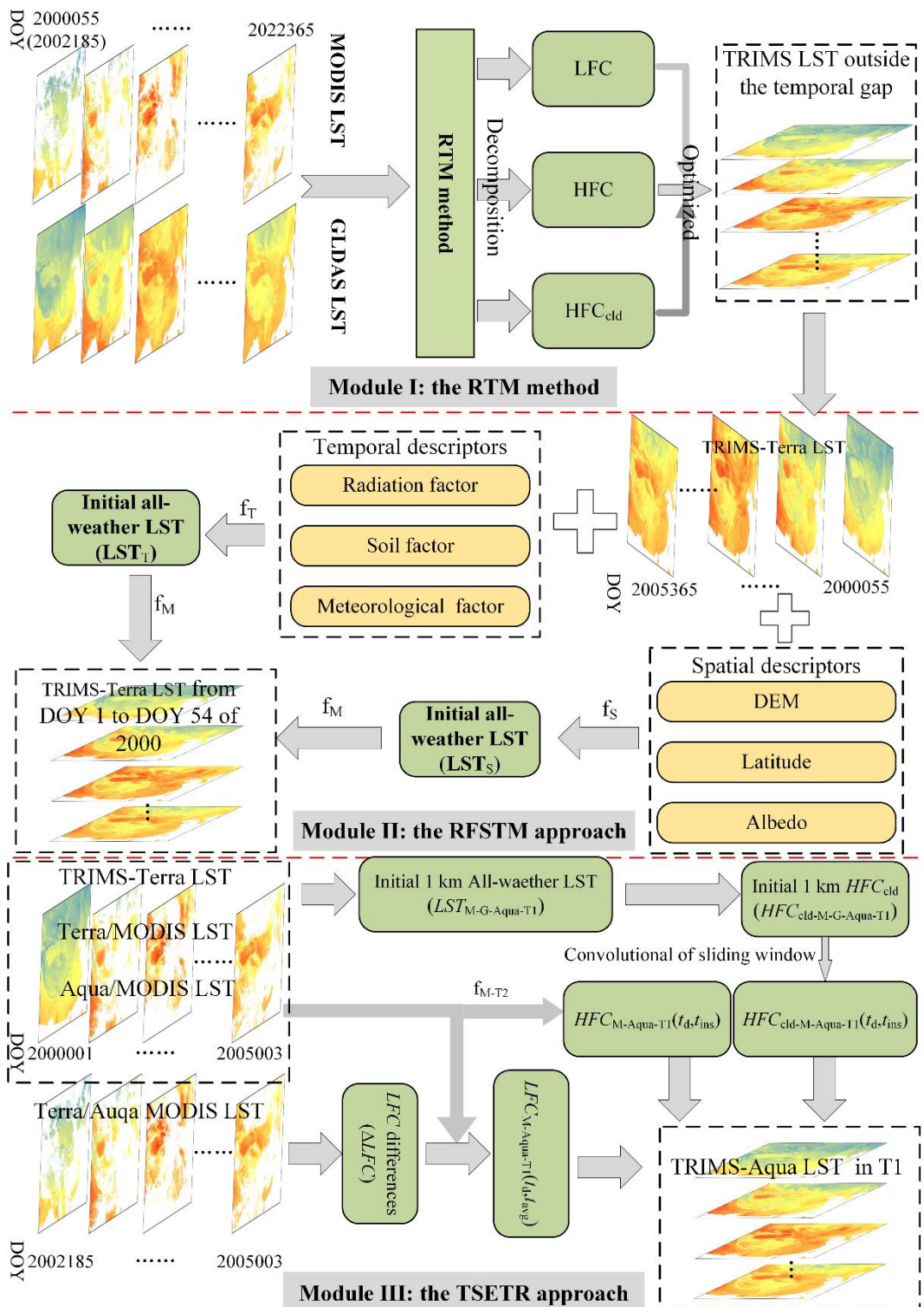
Figure 2: Flowchart of the E-RTM method. Note that the date in this figure is in the format of YYYY+DOY.

199   In the temporal stage, the daily LST ($\mathbf{LST}_T$) of a pixel Q in a certain period are modelled as:

200    $$\begin{aligned}
\mathbf{LST}_T &= f_T(\mathbf{X}_T) \\
\mathbf{X}_T &= [\mathbf{P}_{T,1}\ \mathbf{P}_{T,2}\ ...\ \mathbf{P}_{T,m}]^T \\
&= \begin{bmatrix}
P_{T,1}(t_{d,1}) & P_{T,1}(t_{d,2}) & \cdots & P_{T,1}(t_{d,n}) \\
P_{T,2}(t_{d,1}) & P_{T,2}(t_{d,2}) & \cdots & P_{T,2}(t_{d,n}) \\
\cdots & \cdots & & \cdots \\
P_{T,m}(t_{d,1}) & P_{T,m}(t_{d,2}) & \cdots & P_{T,m}(t_{d,n})
\end{bmatrix}
\end{aligned}$$ (2)

201   where the subscript T denotes the temporal stage; the function f_T expresses the mapping in temporal dimensions from
202   descriptors to LST; $\mathbf{X}_T$ denotes the matrix including LST descriptors' time series ($\mathbf{P}_{T,i}$, i=1, 2, ..., m); and n is the number of
203   days within the temporal gap of Terra MODIS LST.
204   Since the MODIS LST is not available as a reference for reconstruction and it is impossible to identify the different weather
205   conditions (e.g., clear-sky and cloudy conditions), we used the mapping function f_T to predict the 1-km all-weather LST.
206   However, the relationship between LST and its descriptors cannot be analytically expressed currently. Fortunately, the machine
207   learning has been reported to be effective in enhancing the spatial resolution of remote sensing images. Specifically, the random
208   forest (RF) algorithm has shown good performance in mapping the correlation between LST with finer resolution and its
209   descriptors with coarser resolution (Xiao et al., 2023; Li et al., 2021a; Xu et al., 2021; Zhao and Duan, 2020; Yoo et al.,2020).
210   Therefore, the RF algorithm was employed here to realize f_T. The temporal descriptors of LST include net longwave radiation,
211   downward longwave flux, soil moisture profile (e.g., surface, 0–10 cm, and 10–40 cm in GLDAS NOAH model-based data),
212   wind-speed, soil temperature profile (e.g., surface, 0–10 cm, and 10–40 cm in GLDAS NOAH-model based data), air
213   temperature, and land surface albedo. The training period for f_T with RF was set as DOY 55 of 2000 to DOY 55 of 2005, and
214   the prediction period for $\mathbf{LST}_T$ was from DOY 1 of 2000 to DOY 54 of 2000.
215   Considering that LST varies in both temporal and spatial dimensions, the spatial descriptors of LST should also be considered.
216   In the spatial stage, the LST ($\mathbf{LST}_S$) at t_d in the prediction period are expressed as:

217    $$\mathbf{LST}_S = f_S[N_{S,1}(t_d)\ N_{S,2}(t_d)\ ...\ N_{S,k}(t_d)],$$ (3)

218   where the subscript S denotes the spatial stage; the function f_S expresses the mapping in spatial dimensions from the descriptors
219   to LST; k is the number of spatial descriptors of LST; and N_S denotes the 1-km spatial descriptor of LST ($N_{S,i}$, i=1, 2, ..., k).
220   The spatial descriptors of LST include the DEM, latitude, and albedo. The selected descriptors in the spatial stage are all from
221   the ancillary data with a 1-km resolution. Albedo serves as a descriptor that informs about land surface, including factors such
222   as vegetation growth, surface/sub-surface moisture distribution, and land surface cover type.
223   To involve all spatio-temporal LST descriptors and guarantee the best performance of the output, the LST ($\mathbf{LST}_T$ and $\mathbf{LST}_S$)
224   need to be merged together to derive the final 1-km LST ($\mathbf{LST}_M$):

225    $$\mathbf{LST}_M = f_M(\mathbf{LST}_T, \mathbf{LST}_S),$$ (4)

226   where f_M denotes the RF-based mapping which indicates the contributions to the $\mathbf{LST}_M$ from $\mathbf{LST}_T$ and $\mathbf{LST}_S$, respectively.

227 For a single 1-km pixel, the RF-based regression contribution function is trained using $\mathbf{LST_T}$ (obtained by Eq. 2), $\mathbf{LST_S}$
228 (obtained by Eq. 3) and TRIMS LST in the training period. Then, f_C is applied to estimate the 1-km all-weather LST in the
229 prediction period via Eq. (4).

3.3 Module III: the TSETR approach

231 The TSETR approach was developed to estimate the all-weather LST during the period from DOY 1 of 2000 to DOY 184 of
232 2002 during which the Aqua/MODIS LSTs were not available (with a temporal gap of 915 days). Previous studies have shown
233 that it is possible to convert between the Terra MODIS LST and Aqua MODIS LST, considering land cover types, geolocation,
234 and season (Coops et al., 2007). Therefore, Terra/MODIS LST from 2000-2002 could be transformed to Aqua/MODIS LST
235 (Li et al., 2018). Since the Terra/MODIS LST (MOD11A1) is available as a reference in the temporal gap, we generated an
236 all-weather LST based on the TSETR approach, which is reconstruction rather than prediction.
237 According to Eq. (1), the LST time series can be decomposed into *LFC*, *HFC*, and *HFC*$_{cld}$ under all-weather conditions.
238 Therefore, the TSETR approach has three stages. In the first stage, we need to estimate the *LFC* during the temporal gap at the
239 Aqua overpass time. In this case, the temporal gap period was set as T1, and DOY 185 of 2002 to DOY 3 of 2005 was set as
240 T2 (Fig.3). According to the analytical expression and physical meaning of *LFC*, there is no underlying trends of change within
241 the three annual parameters (T_{avg}, A and ω) except for the periodic variation in the LST, which means that the *LFC* is cyclic-
242 stationary over a short time period (Bechtel, 2015; Weng and Fu, 2014; Zhu et al., 2022). Once the three annual parameters
243 are determined, the *LFC* can be calculated for a given day.
244 Therefore, in the TSETR approach, we assume that the *LFC* differences (ΔLFC) between the Terra and Aqua overpass times
245 in T1 and T2 are also cyclic-stationary. In T2, the *LFC* at the Terra/MODIS and Aqua/MODIS pixels are determined separately.
246 In T1, the *LFC* at the Aqua overpass time of the pixel M can be expressed as:

247
$$
\begin{cases}
LFC_{\text{M-Aqua-T1}}(t_d, t_{avg}) = LFC_{\text{M-Terra-T1}}(t_d, t_{avg}) + \Delta LFC_M(t'_d, t_{avg}) \\
\Delta LFC_M(t'_d, t_{avg}) = LFC_{\text{M-Aqua-T2}}(t'_d, t_{avg}) - LFC_{\text{M-Terra-T2}}(t'_d, t_{avg})
\end{cases}
\tag{5}
$$

248 where t_d is a specific day in T1; t'_d is a specific day corresponding to t_d in T2; $LFC_{\text{M-Aqua-T1}}(t_d, t_{avg})$ and $LFC_{\text{M-Terra-T1}}(t_d, t_{avg})$
249 denote the *LFC* corresponding to the Aqua/Terra overpass time in T1, respectively; and $LFC_{\text{M-Aqua-T2}}(t'_d, t_{avg})$ and $LFC_{\text{M-Terra-}}$
250 $_{\text{T2}}(t'_d, t_{avg})$ denote the *LFC* corresponding to the Aqua and Terra overpass time in T2, respectively.

11
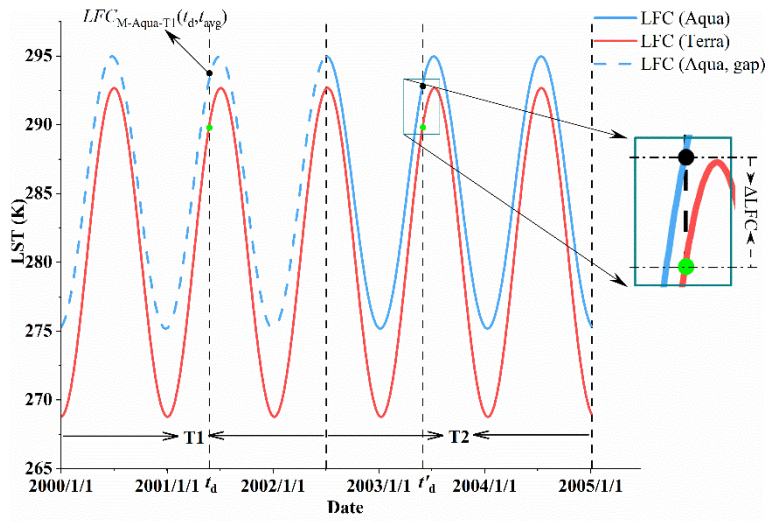
Figure 3: Schematic diagram for estimating *LFC* at daytime Aqua overpass time in T1.

HFC is estimated in the original RTM method using a nonlinear mapping established by multiple descriptors. In the second stage of E-RTM, the *HFC* within T1 at the Aqua overpass time can be estimated by using its descriptors through RF (Xu et al., 2021). With Module I and Module II, we have obtained TRIMS-Terra LST in T1. However, it is unfeasible to directly model an RF mapping based on Terra MODIS data and its corresponding descriptors in T1. An important concern that needs to be addressed is the timing discrepancy between Terra and Aqua observations, which results in distinct variations in the pattern of LST changes. When there is no valid Aqua LST available, we have made improvements to the procedure for calculating the HFC in the original RTM method as follows:

$$
\begin{cases}
HFC_{M\text{-}Aqua\text{-}T1}(t_d, t_{ins\text{-}Aqua\text{-}T1}) = HFC_{M\text{-}Terra\text{-}T1}(t_d, t_{ins\text{-}Terra\text{-}T1}) + \Delta HFC_{M\text{-}Terra\text{-}Aqua\text{-}T1} \\
\Delta HFC_{M\text{-}Terra\text{-}Aqua\text{-}T1}(t_d, t_{ins}) = f_{M\text{-}T2}(g_M, DEM_M, NDVI_M(t_d), slp_M(t_d), \alpha_M(t_d), v_M(t_d), \Delta LFC_M, \Delta DTC_M) \\
\Delta DTC_M = \Delta DTC_{M\text{-}Aqua}(t_d, t_{ins}, t_{avg}) - \Delta DTC_{M\text{-}Terra}(t_d, t_{ins}, t_{avg})
\end{cases}
\tag{6}
$$

where ΔLFC characterizes the systematic deviation of the steady state component; g_M is geo-spatial code (Yang et al.,2022); DEM_M, $NDVI_M$, slp_M, α_M, Δt_M and v_M are the latitude, longitude, DEM, NDVI, slope, albedo, difference between t_{ins} and t_{avg}, and the atmospheric water vapour content, respectively; ΔDTC characterizes the warming effect of solar radiation, and the weather effect can be characterized by the atmospheric water vapor content. According to Zhang et al. (2021), the HFC characterizes the change in LFC with ΔDTC and WTC superimposed under ideal clear-sky conditions. The detailed calculation of ΔDTC can be found in Zhang et al. (2019).

The $f_{M\text{-}T2}$ is constructed as follows. Initially, the correlation image of the target pixel M is determined within the T2 time period and the following two conditions need to be satisfied by the correlation image: (i) the mean bias deviation (MBD) of the DTC estimated from its corresponding GLDAS LST (10:00-14:00 and 21:00-3:00 local solar time) should be lower than 1 K, and (ii) the difference in the average observation time between the GLDAS pixels should not exceed 0.5 h. Using the correlation

image, the similar image family S of the target pixel M is determined. Subsequently, in the correlation image, using similar land surface type criteria, the similar image family S of the target pixel M within the GLDAS pixels is identified. S needs to meet the following two conditions: (i) it should have the same surface type as M and (ii) the R of the Terra-MODIS LST time series corresponding to S and M need to be greater than 0.8.

In the third stage, we need to estimate the HFC_{cld} within the temporal gap period at the Aqua overpass time. In fact, HFC_{cld} is essentially an atmospheric correction term and it is obtained from the GLDAS LST in the RTM method. According to the parameterization scheme of the RTM method, the clear-sky MODIS pixels and their corresponding GLDAS LST are the necessary inputs for the estimation of HFC_{cld}. It is not possible to obtain HFC_{cld} directly in this stage due to the lack of Aqua/MODIS in T1.

Inspired by the Temporal Component Decomposition (TCD) method (Zhang et al., 2019b) and other methods integrating PMW and TIR LST (Parinussa et al., 2016; Zhang et al., 2020), the initial value of the 1-km HFC_{cld} can be expressed as:

$$HFC_{cld\text{-}M\text{-}G\text{-}Auqa\text{-}T1}(t_d, t_{ins}) = LST_{M\text{-}G\text{-}Auqa\text{-}T1}(t_d, t_{ins}) - LFC_{M\text{-}Auqa\text{-}T1}(t_d, t_{avg}) - HFC_{M\text{-}Auqa\text{-}T1}(t_d, t_{ins}), \tag{7}$$

where $HFC_{cld\text{-}M\text{-}G\text{-}Aqua\text{-}T1}$ is the initial 1-km HFC_{cld} of M; and $LST_{M\text{-}G\text{-}Aqua\text{-}T1}$ is the initial 1-km LST of M under all-weather conditions.

Based on the findings of Yao et al. (2023), we established the method for acquiring the initial 1-km all-weather LST. Initially, the GLDAS LST that corresponded to the Aqua overpass time are corrected for systematic bias using the cumulative distribution function matching (Xu and Cheng., 2021). In T1 time period, since Aqua LST is unavailable, we employee MODIS LST from 2003-2022 to guarantee an adequately large sample size of MODIS LST. We then downscaled the GLDAS LST to 1 km through the following two steps.

(i) Calculating the LST differences between the MODIS and GLDAS:

$$\begin{cases} \Delta LST_{M\text{-}G\text{-}Auqa\text{-}T1}(t_d, t_{ins}) = LST_{G\text{-}Auqa\text{-}T1}(t_d, t_{ins}) - LST_{M\text{-}Auqa\text{-}T1}(t_d, t_{ins}) \\ LST_{M\text{-}Auqa\text{-}T1}(t_d, t_{ins}) = LFC_{M\text{-}Auqa\text{-}T1}(t_d, t_{ins}) + HFC_{M\text{-}Auqa\text{-}T1}(t_d, t_{ins}) \end{cases}, \tag{8}$$

where $LST_{G\text{-}Aqua\text{-}T1}$ is GLDAS LST; $LST_{M\text{-}Aqua\text{-}T1}$ is ideal MODIS clear-sky LST. $LST_{M\text{-}G\text{-}Aqua\text{-}T1}$ is LST difference image. One pixel in GLDAS LST corresponds to 625 (25 × 25) pixels in MODIS LST. The LST differences are calculated as GLDAS LST minus 625-pixel average MODIS LST. LST difference image was then directly resampled to 1 km.

(ii) Downscaling of GLDAS LST:

$$LST_{M\text{-}G\text{-}Auqa\text{-}T1}(t_d, t_{ins}) = \Delta LST_{M\text{-}G\text{-}Auqa\text{-}T1}(t_d, t_{ins}) + LST_{M\text{-}Auqa\text{-}T1}(t_d, t_{ins}), \tag{9}$$

where $LST_{M\text{-}G\text{-}Aqua\text{-}T1}$ is the initial 1-km downscaled GLDAS LST. The heterogeneity of the underlying land surface within a 0.25° grid is reflected by MODIS LST, and the downscaled GLDAS LST also exhibits the same characteristic. This is based on the hypothesis that the spatial variations in MODIS LST is the same as that of GLDAS LST. However, $LST_{M\text{-}G\text{-}Aqua}$ and $HFC_{cld\text{-}M\text{-}G\text{-}Aqua\text{-}T1}$ in the results of Eq. (9) may still contain systematic errors due to inadequate downscaling (Eq. 8). Therefore, a convolutional implementation of a sliding window was used here to reduce the systematic error contained in $HFC_{cld\text{-}M\text{-}G\text{-}Aqua\text{-}T1}$ (Chen et al., 2011; Wu et al., 2015; Zhang et al., 2019b).

303   The schematic diagram of the convolutional implementation of the sliding window is shown in Fig.4. To fully reduce the

304   systematic bias, the size of the sliding window should be slightly larger than a GLDAS pixel (26×26 km^2). According to

305   Zhang et al. (2019, 2021), HFC_{cld} after optimization of M (i.e., HFC_{cld} after eliminating the systematic errors) can be obtained

306   by convolving the HFC_{cld} of the surrounding similar pixels by combining geological factors (e.g., land surface type, spatial

307   distance, and topography). This method is based on the interrelationship of different LST: neighbouring HFC_{cld} are correlated

308   in a limited spatial domain. Previous studies have shown that the approaches analogous to the convolutional implementation

309   of sliding windows have a good ability to improve both the accuracy and the image quality of the merged LST (Ding et al.,

310   2022; Long et al., 2020; Zhang et al., 2019b). Similar pixels (termed as S) need to meet the following criteria: (i) they are

311   within the same sliding window as the target pixel, and (ii) their land cover type does not differ from the target pixel. Therefore,

312   the target pixel itself is also a reference pixel. Eventually, the HFC_{cld} of target pixel can be expressed as:

313
$$HFC_{cld\text{-}M\text{-}Aqua\text{-}T1}(t_d, t_{ins}) = \sum_{i=1}^{n} HFC_{cld\text{-}S_i}(t_d, t_{ins}) \cdot w_{S_i} , \tag{10}$$

314   where n is the number of similar pixels; $HFC_{cld\text{-}S}$ denotes $HFC_{cld\text{-}M\text{-}Aqua\text{-}T1}$ of the similar pixels; and w_s is the contribution of

315   similar pixels to M, which can be expressed as:

316
$$\begin{cases} w_{S_i} = D_{S_i} \cdot H_{S_i} \cdot N_{S_i} \Big/ \left(\sum_{n} D_{S_i} \cdot H_{S_i} \cdot N_{S_i} \right) \\[2mm] D_{S_i} = (1/d_{S_i}) \Big/ \sum_{i=1}^{n} 1/d_{S_i} \\[2mm] d_{S_i} = \sqrt{(x_{S_n} - x_M)^2 + (y_{S_n} - y_M)^2} \\[2mm] H_{S_i} = \left| DEM_{S_i} - DEM_M \right| \\[2mm] N_{S_i} = \left| NDVI_{S_i} - NDVI_M \right| \end{cases} , \tag{11}$$

317   where D_S, H_S and N_S are the differences between the similar pixels and M in terms of the spatial distance, DEM and NDVI,

318   respectively.
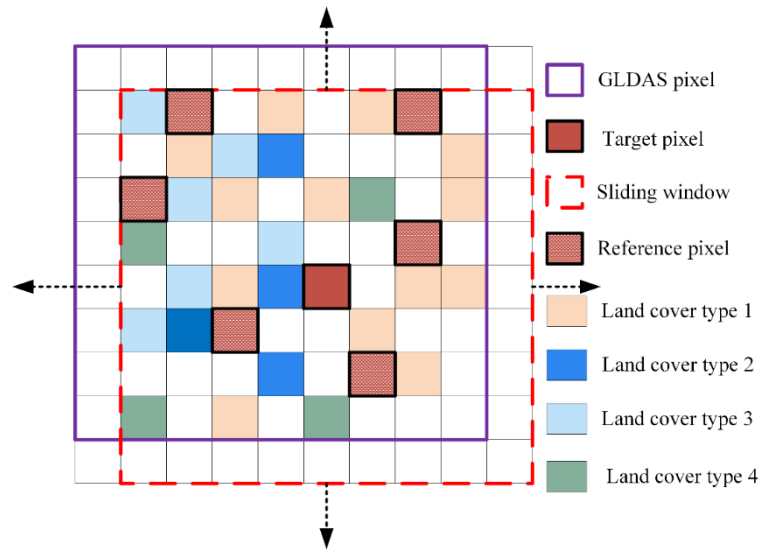
Figure 4: Schematic of the *HFC*_cld convolutional optimization.

3.4 Implementation of E-RTM

A detailed description of the implementation process of the RTM method is provided by Zhang et al. (2021) and is not repeated here. The implementation process of Module II and Module III is explained in this section.

Stage I: Data preprocessing and spatiotemporal matching

In this stage, the data are preprocessed and spatiotemporal matching. First, valid MODIS LST are selected with the following two standards: (i) the quality control of the pixel was flagged as "good" and (ii) the view angle of the pixel was lower than 60°. Second, the selected temporal descriptors from GLDAS data were temporally interpolated using the cubic spline function to observation time of MODIS LST for the purpose of temporal-matching. Third, the observation times for cloudy pixels and temporal gaps were recovered using a 16-day revisiting period. Fourth, the 90-m DEM, 500-m albedo, and 500-m NDSI were upscale to 1-km to match the MODIS LST. Fifth, he GLDAS water vapor were extended to 1 km by cubic convolution interpolation. During the temporal gap (DOY 1–54 2000), SPOT VGT served as the NDVI, GLASS albedo was extended to a 1 km resolution using cubic convolution interpolation, and the NDSI was determined by taking the average of the corresponding days in 2001 and 2002. The 16-day 1-km NDVI are temporally interpolated to daily resolution. The daily missing albedo caused by cloud-coverage are filled up through Statistics-based Temporal Filter (Liu et al., 2013a). In addition, all data are spatially matched.

Stage II: Implementation of the RFSTM

(1) For a single 1-km pixel, training the RF regression relationship (i.e., f_T) between TRIMS-Terra LST and the temporal descriptors from GLDAS data via Eq. (2). The RF parameters were set as follows: n estimators=420, max depth=43, max features=9, and min samples leaf=1. In the temporal stage of RFSTM, all-weather samples from 2000 to 2005 were compiled. Two-thirds of the samples are used for model training and the remaining are for model validation (Breiman, 2001).

15

(2) For a specific day (t_d), using the 1-km NDVI (Sobrino et al.,2004) and NDSI to classify the study area into several subareas, including thick vegetation (NDVI>0.5), sparse vegetation (0.2≤NDVI≤0.5), barren land areas (NDVI<0.2), and snow-ice areas (NDSI>0.1) (Zhang et al., 2019a) and water (NDVI<0). Then, for each subarea, the spatial descriptors of LST are input into f_S via Eq. (3). Note that f_S with RF is trained with the 1-km LST and spatial descriptors of a day, with the same observation time as t_d and the smallest difference in the number of days between t_d.

(3) For a single 1-km pixel, train the RF-based regression contribution function (i.e., $\mathbf{f_M}$ in Eq. 4) using $\mathbf{LST_T}$, $\mathbf{LST_S}$, and TRIMS-Aqua LST under clear-sky conditions. Then, estimate the 1-km TRIMS-Aqua LST during the period of DOY 1-54 2000 by applying $\mathbf{f_M}$ to clear-sky and cloudy conditions, respectively.

Stage III: Implementation of the TSETR

1) For a single Aqua-MODIS pixel M in T1, determine its LFC in Eq.(5) using Aqua-MODIS LST (T2) and Terra-MODIS LST(T1 and T2).

2) Train the RF measuring (f_{M-T2}) between all of ΔHFC and its descriptors (see section 3.3) of all similar pixels. The RF measuring function tools are also provided by the MATLAB platform. The RF parameters were set as follows: n estimators = 100, max depth = 20, max feature = 4, min samples leaf = 1. Determine the reconstructed HFC of M through Eq. (6) by applying the descriptors of HFC in M to f_{M-T2}.

3) Implement the bias correction for GLDAS LST of the target GLDAS grid by using cumulative distribution function matching. Then, downscale the GLDAS LST to 1 km through Eqs.(8) and (9).

4) Determine the initial 1-km HFC_{cld} of M through Eq.(7).Finally, determine the HFC_{cld} of M through Eqs.(10) and (11).

3.5 Evaluation strategies

As can be seen from Fig. 2, TRIMS LST can be divided into two parts according to the period of data coverage: data within the temporal gap period and data outside the temporal gap period. There are differences in the evaluation strategies within the two periods due to the different availability of validation data.

For outside the temporal gap period, the TRIMS LST was compared with LSTs derived from two reanalysis datasets (i.e., GLDAS and the independent ERA5-Land) and retrievals from two different satellite TIR sensor (i.e., MODIS and the independent AATSR). In comparing different LSTs, samples with time differences greater than five minutes were excluded (Freitas et al., 2010; Göttsche et al., 2016; Jiang and Liu, 2014). The quantitative metrics used in comparison analyses include the MBD, STD of bias, and coefficient of determination (R^2). Then, the TRIMS LST was validated under different weather conditions based on *in-situ* LST from the ground sites listed in Table I. The three metrics used the mean bias error (MBE), root-mean-square-error (RMSE), and R^2.

During the temporal gap period, the TRIMS LST was tested using two methods. Firstly, the results of the original RTM method were cross-referenced and validated empirically with RFSTM and TSETR. In 2003, RFSTM was utilized to merged GLDAS and Terra MODIS data, resulting in a 1-km all-weather LST. Additionally, the TSETR method was employed to generate TRIMS-Aqua LST for the periods of 2003–2005 and 2013–2015. For the actual data generated for the period 2000-2002,

374 specifically Aqua LST, the similarity of the TRIMS LST time series was quantified to examine the reliability of TRIMS LST

375 during the Aqua/MODIS temporal gap. The time series angle (TSA), inspired by the spectral angle that is widely used to

376 measure the similarity between spectral curves (Kruse et al., 1993), was used to quantify the similarity of TRIMS LST time

377 series. The TSA is defined as:

378 $$\theta = \cos^{-1}\frac{\mathbf{LST}_{\text{TRIMS-Aqua}} \bullet \mathbf{LST}_{\text{TRIMS-Terra}}}{\left\|\mathbf{LST}_{\text{TRIMS-Aqua}}\right\| \cdot \left\|\mathbf{LST}_{\text{TRIMS-Terra}}\right\|} , (12)$$

379 where θ is the TSA (unit: degree); $\mathbf{LST}_{\text{TRIMS-Aqua}}$ and $\mathbf{LST}_{\text{TRIMS-Terra}}$ are time series of TRIMS-Aqua and TRIMS-Terra LSTs,

380 respectively. From this formula, we know that smaller TSA denotes higher similarity.

381 Based on the CLCD described in Section 2.1, six subareas with a single land cover type and no land cover change in T1 and

382 T2 (January 1 2000 to January 3 2005) were selected to extract the corresponding TRIMS-Terra and TRIMS-Aqua LST time

383 series. These six subareas (Fig.1) were recorded as A (82.30°N–83.16°N, 39.63°E–40.03°E, barren land), B (124.73°N–

384 125.17°N, 51.51°E–51.95°E, forest), C (111.84°N–112.30°N, 42.47°E–42.85°E, grassland), D (100.78°N–101.53°N, 39.92°E

385 –40.44°E, barren land), E (98.14°N–98.61°N, 33.92°E–34.25°E, grassland), and F (91.73°N–92.22°N, 31.7°E–32.01°E,

386 grassland). Then, the TSA was calculated to quantify the similarity between the TRIMS-Terra and TRIMS-Aqua LST time

387 series.

388 **4. Results and discussion**

389 **4.1 Comparison of the TRIMS LST with reanalysis data**

390 With the E-RTM method, TRIMS LST products from January 1 2000 to December 31 2022 were generated. The spatial

391 resolution was 1 km. The temporal resolution was four observations per day, which is the same as the overpass time of

392 Terra/MODIS and Aqua/MODIS. Fig. 5 shows the daytime TRIMS-Aqua LST on DOY 1, 91, 181, and 271 as examples.

393 Fig. 5 shows that the TRIMS-Aqua LST has a similar spatial pattern as the GLDAS LST since the latter is an input for the

394 former. Good agreement in the spatial pattern in different seasons can also be observed between TRIMS-Aqua LST and the

395 independent ERA5-Land LST. A careful observation of Fig.4 demonstrates that the TRIMS LST is spatially seamless and its

396 spatial patterns are as expected. Southern China as well as southeast Asia and the south Asian subcontinent in low latitudes

397 are warm in all seasons because of additional absorbed solar radiation. The Tibetan Plateau, with much higher elevation and

398 the regions in high latitudes is much cooler than other regions. In spring (DOY 1), summer (DOY 181), and autumn (DOY

399 271), northwestern China, where the dominant land cover type is barren land, is much warmer than other regions. Further

400 comparison indicates that TRIMS LST is generally slightly warmer than the GLDAS LST and the ERA5-Land LST. For

401 example, on DOY 1 of 2000, the LST are generally below 278 K in the eastern Tibetan Plateau, while the GLDAS LST and

402 the ERA5-Land LST are approximately 3–5 K lower. In the generation scheme of the TRIMS LST, the MODIS LST, which

17

403 is generally warmer than the LST provided by reanalysis data, is an important input as well as a reference to 'calibrate' the
404 GLDAS LST. This induces the 'merged' TRIMS LST to be warmer than the GLDAS LST as well as the ERA5-Land LST.
405
406
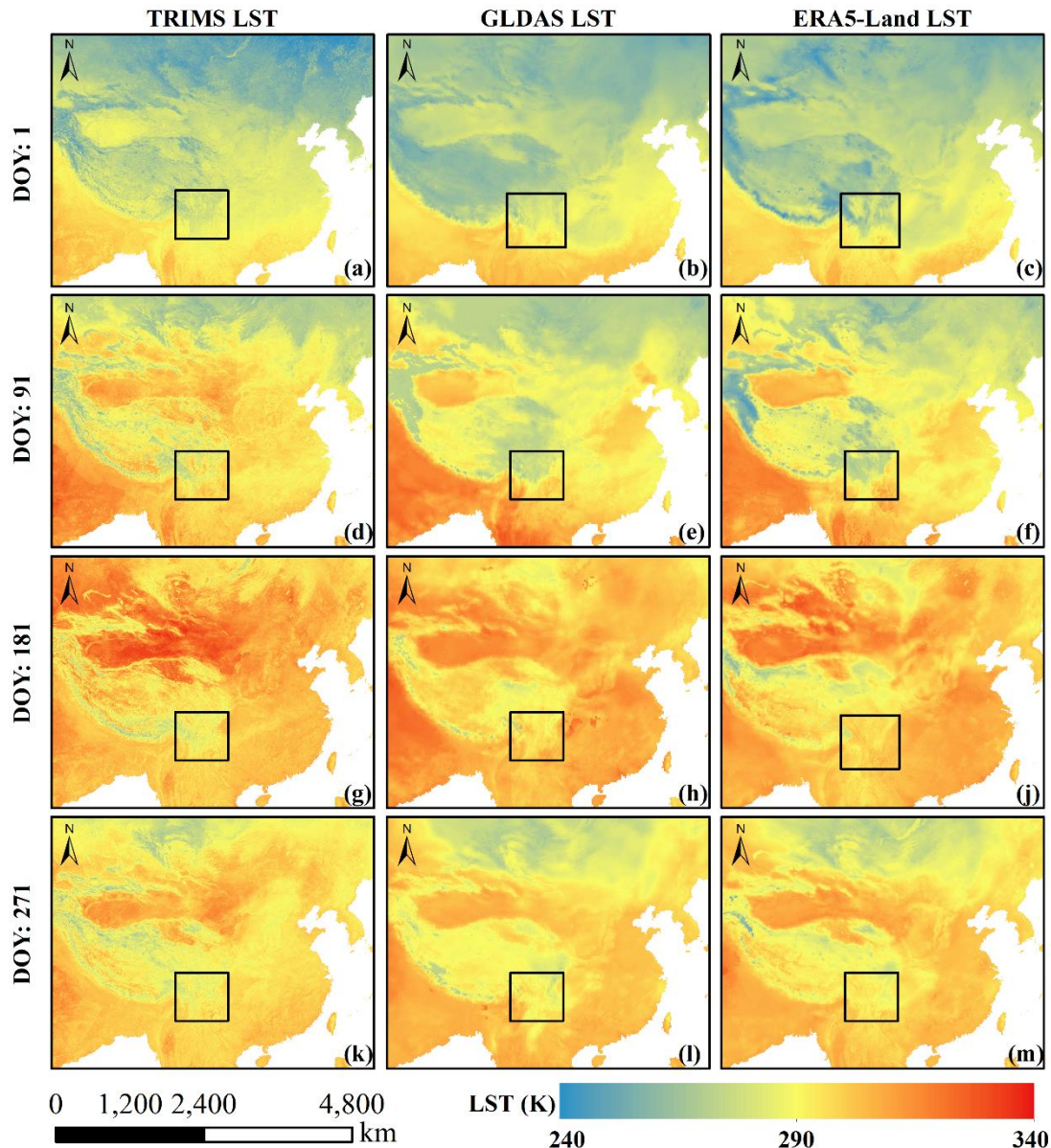
Figure 5: Spatial patterns of the daytime TRIMS-Aqua LST, GLDAS LST, and ERA5-Land LST on four selected days in 2000.

409 To further examine the image quality of the TRIMS-Aqua LST, Fig. 6 shows the daytime TRIMS-Aqua LST, GLDAS LST,
410 and ERA5-Land LST of the subarea shown in Fig. 5 at the Aqua overpass time in 2000. Compared with the GLDAS LST and
411 the ERA5-Land LST, the TRIMS LST offers more spatial details because of its much higher spatial resolution. Thus, one can

18

see clear terrain-induced temperature variations. Furthermore, Fig. 6 shows that no evident spatial discontinuities exist in the TRIMS LST, indicating the E-RTM method performs satisfactorily in addressing the spatial scale mismatch between the MODIS LST and GLDAS LST (Zhang et al., 2021).
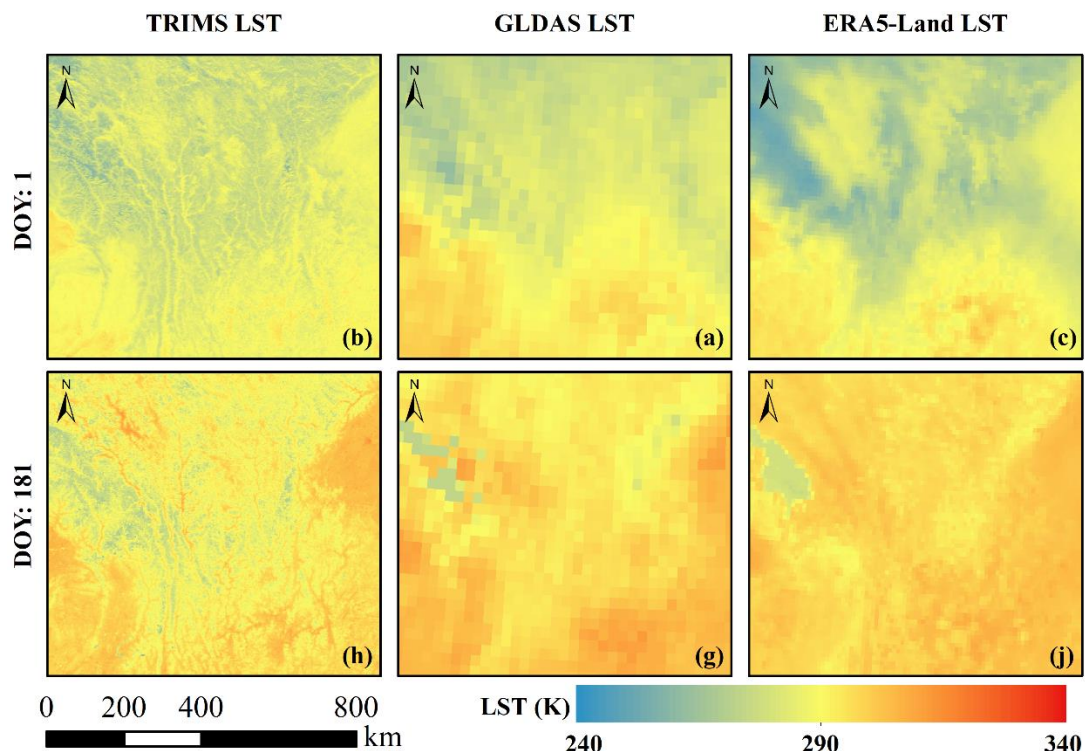

Figure 6: The daytime TRIMS-Aqua LST, GLDAS LST, and ERA5-Land LST of the subarea (shown in Fig.5) in 2000.

4.2 Comparison of the TRIMS LST with satellite TIR LST products

The daily TRIMS LST was compared with the independent ENVISAT/AATSR LST (from 2004 to 2012) and the Terra/Aqua MODIS LST (from 2000 to 2021 for Terra and from 2002 to 2021 for Aqua). Note that the AATSR and MODIS only have clear-sky LST. The density plots are shown in Fig.7. To facilitate the data processing and presentation, 1%/1‰ matched TRIMS-AATSR/MODIS pairs were randomly extracted. Fig. 7 indicates good consistency between the TRIMS LST and AATSR/MODIS LST. Compared with AATSR, the overall MBD/STD values of TRIMS were 0.37 K/1.55 K and -0.44 K/1.22 K for daytime and nighttime, respectively; compared with MODIS, the overall MBD/STD values were 0.09 K/1.45 K and -0.03 K/1.17 K for daytime and nighttime, respectively. Fig. 7 also shows that better agreements exist during nighttime because of lower thermal heterogeneity.

19
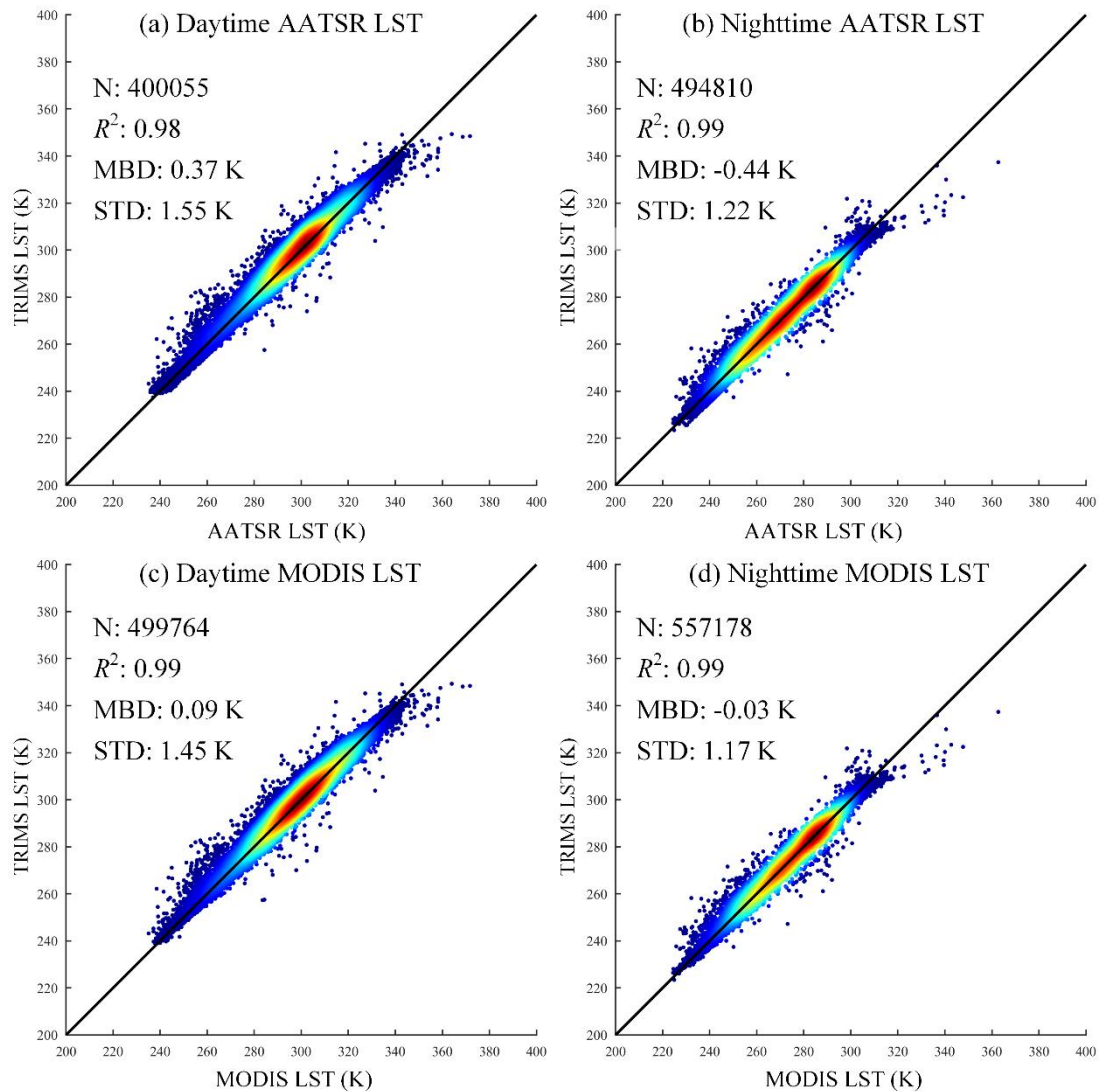
Figure 7: Density plots between the TRIMS LST and the AATSR/MODIS LST.

To further examine the deviation of the TRIMS LST from the AATSR/MODIS LST, the MBD and STD values were calculated for each day. Fig. 8 shows the corresponding histograms. For AATSR, the daily daytime MBD and STD were mainly concentrated in the ranges of 0 K–0.60 K and 1.05 K–1.15 K, respectively; the daily nighttime MBD and STD were mainly concentrated in the ranges of -0.40 K to 1.0 K and 0.75 K to 1.15 K, respectively. The positive deviation and negative deviation were consistent with those in Fig.8 (a) and Fig.8 (b). For the MODIS case, the daytime MBD was concentrated between -0.6 K and 1.0 K, and STD was concentrated between 1.0 K and 2.50 K; the nighttime MBD was concentrated between -0.6 K and 0.3 K and STD was concentrated between 0.9 K and 1.50 K. As shown above, it should be concluded that the daily differences between the long-term TRIMS LST and AATSR/MODIS LST remain stable.

20
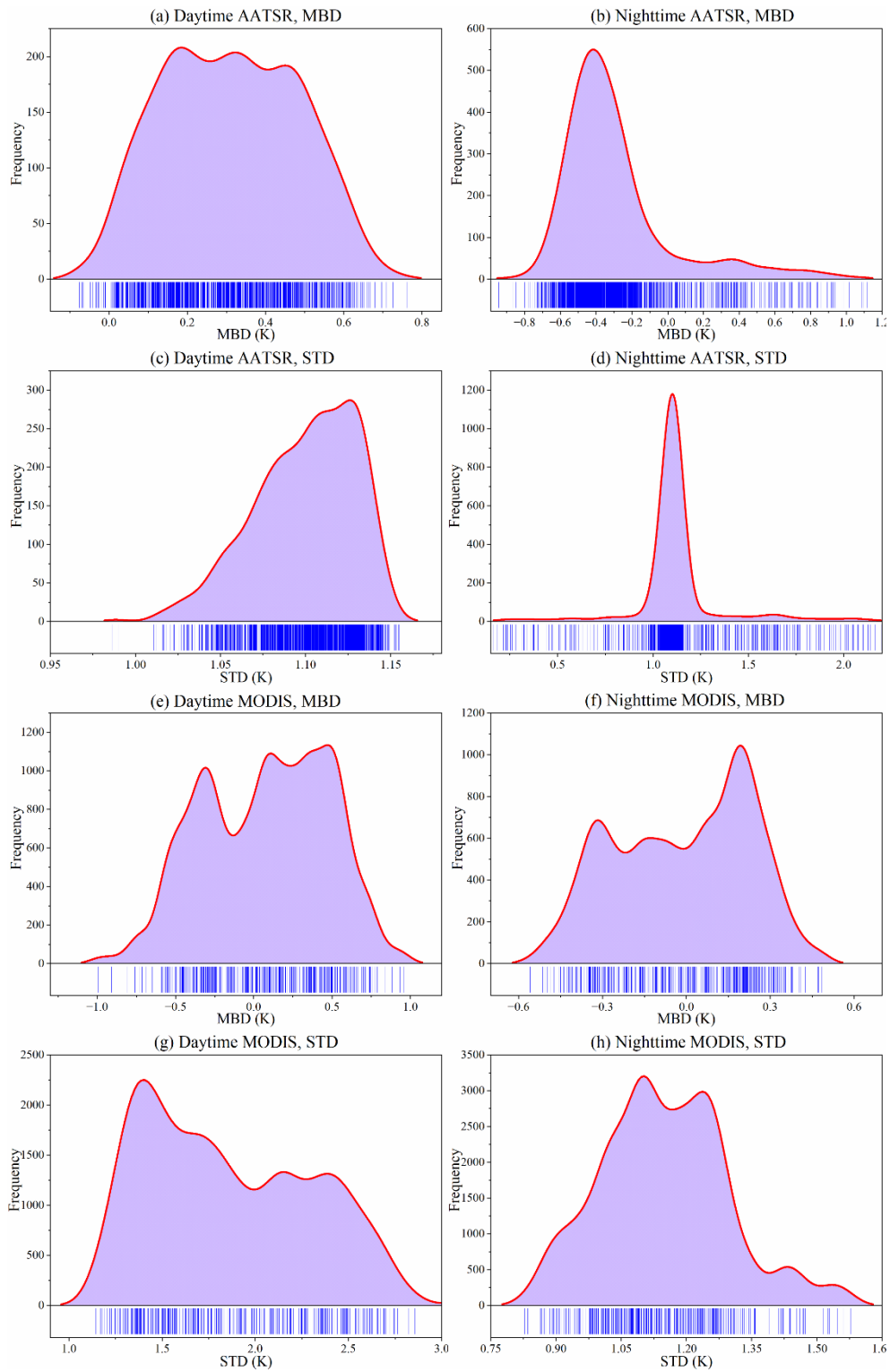
437
438 **Figure 8: Histograms of the MBD and STD to compare the TRIMS LST and the AATSR/MODIS LST.**

4.3 Validation against *in-situ* LST outside the temporal gap

The TRIMS LST was quantitative validated against the *in-situ* LST. Remove anomalies caused by transient environmental factors based on 3σ (standard deviation) filtering (Göttsche et al., 2016; Yang et al., 2020). It should be noted that the results for all sites can be found in Tables B1 and B2. The nineteen ground sites were divided into four groups according to locations and land cover types (Group I: ARO, D105, DSL, EBA, and MQU; Group II: DET, GAZ, GOB, HZZ, and SSW; Group III: DAM, DXI, GUT, HLA, and TYU; Group IV: CBS, DHS, QYZ, and SDQ). Table II and Table III show the validation results of TRIMS LST against the *in-situ* LST under different sky conditions. In addition, the validation results of the clear-sky MODIS LST are provided for comparison.

Table II: R^2, MBE, and RMSE of the daytime validation for different groups.

Group	Land cover type	Condition	Amounts	TRIMS LST			MODIS LST		
				MBE (K)	RMSE (K)	R^2	MBE (K)	RMSE (K)	R^2
I	Grassland	Clear-sky	5370	0.26	2.15	0.95	0.61	2.37	0.95
		Cloudy	6972	0.41	2.18	0.96	–	–	–
II	Desert or barren land	Clear-sky	5930	0.46	2.30	0.98	0.79	2.53	0.98
		Cloudy	5698	0.43	2.26	0.98	–	–	–
III	Cropland	Clear-sky	5738	0.02	2.11	0.97	-0.21	2.52	0.95
		Cloudy	7570	0.04	2.11	0.97	–	–	–
IV	Forest	Clear-sky	3170	0.55	2.46	0.97	0.72	2.38	0.98
		Cloudy	3655	0.68	2.27	0.98	–	–	–

Table III: R^2, MBE, and RMSE of the nighttime validation for different groups.

Group	Land cover type	Condition	Amounts	TRIMS LST			MODIS LST		
				MBE (K)	RMSE (K)	R^2	MBE (K)	RMSE (K)	R^2
I	Grassland	Clear-sky	8175	-0.70	1.65	0.98	-0.99	1.69	0.98
		Cloudy	5254	-0.13	1.64	0.97	–	–	–
II	Desert or barren land	Clear-sky	6095	-0.64	1.43	0.99	-0.67	1.53	0.99
		Cloudy	5244	-1.17	1.85	0.99	–	–	–
III	Cropland	Clear-sky	5314	-0.83	1.76	0.98	-0.75	1.60	0.98
		Cloudy	7243	-0.60	1.74	0.98	–	–	–
IV	Forest	Clear-sky	2800	-0.98	1.92	0.98	-0.97	2.09	0.98

		Cloudy	3332	-0.94	1.90	0.99	–	–	–

Under clear-sky conditions, the TRIMS LST had an accuracy close to that of the MODIS LST as shown in Table II and Table III. The MBE of the TRIMS LST ranged from -0.98 K to 0.68 K and the RMSE is 1.43 K to 2.46 K. The RMSE of the TRIMS LST under clear-sky conditions is lower than that of the MODIS LST, except for Group IV. The RMSEs of the MODIS LST were reduced by 0.22 K (Group I), 0.23 K (Group II), and 0.41 K (Group III), respectively. The nighttime results were generally better than the daytime results, with an average RMSE of 1.74 K. The R^2 of the TRIMS LST for the four groups of sites were higher than 0.95 under clear-sky conditions, indicating that the TRIMS LST is in good agreement with the *in-situ* LST. The improved accuracy of the TRIMS LST may be due to the reduction of the systematic bias of the original MODIS LST in the E-RTM method by extracting the LFC and HFC (Ding et al., 2022).

Under cloudy conditions, the accuracy of TRIMS LST is slightly lower compared to clear-sky conditions, resulting in a 0.35 K increase in the overall RMSE.

For TRIMS LST under cloudy conditions, the accuracy is marginally below that under clear-sky conditions, and the overall RMSE increased by 0.35 K. For the four groups of sites, the MBE values of TRIMS LST were -0.13 K (Group I), -1.17 K (Group II), -0.60 K (Group III), and -0.94 K (Group IV), revealing that the TRIMS LST is underestimated under cloudy conditions. According to the parameterization scheme of the E-RTM method, the accuracy of the estimated HFC_{cld} under cloudy conditions is affected by the GLDAS LST, which has a negative deviation from the MODIS LST as shown in Section 4.1. In contrast, Although the GLDAS LST is bias-corrected, uncertainty may still exist, which are ultimately detrimental to the accurate recovery of the LST for the cloud-contaminated region. Overall, the validation results indicate that TRIMS LST has good accuracy under cloudy conditions as well as under clear-sky conditions.

For ground sites in Group III with a dominant land cover type of desert or barren land, the nighttime validation shows that the TRIMS-Aqua LST is systematically underestimated, with an MBE of -1.17 K to -0.64 K. After checking the calculated STD, we believe the spatial scale mismatch between the ground site and the pixel is not the main reason for the systematic underestimation. Further examination shows that the clear-sky MODIS LST is significantly underestimated: the MBEs of Aqua/MODIS LST are -1.88 K, -1.03 K, -1.33 K, and -0.60 K for GOB, HZZ, SSW, and GAZ, respectively. Such a cold bias in arid and semiarid regions is also been reported by Li et al. (2019) for the MYD11 LST product. The above results indicate that the accuracy of TRIMS LST is largely dependent on the used MODIS LST.

Reanalysis LST were also validated against *in-situ* LST. GLDAS LST is generally underestimated compared to *in-situ* LST, with MBE of -0.29 K and RMSE of 5.86 K. Under clear-sky and cloudy conditions, the GLDAS LST exhibits MBE values of 0.03 K and -0.62 K, respectively. On the other hand, ERA5-Land LST is overestimated compared with *in-situ* LST, with MBE of 1.60 K and RMSE of 6.37 K. This indicates that the accuracy of the ERA5-Land LST is lower than that of the GLDAS LST. Notably, this discrepancy is more pronounced under clear-sky conditions.
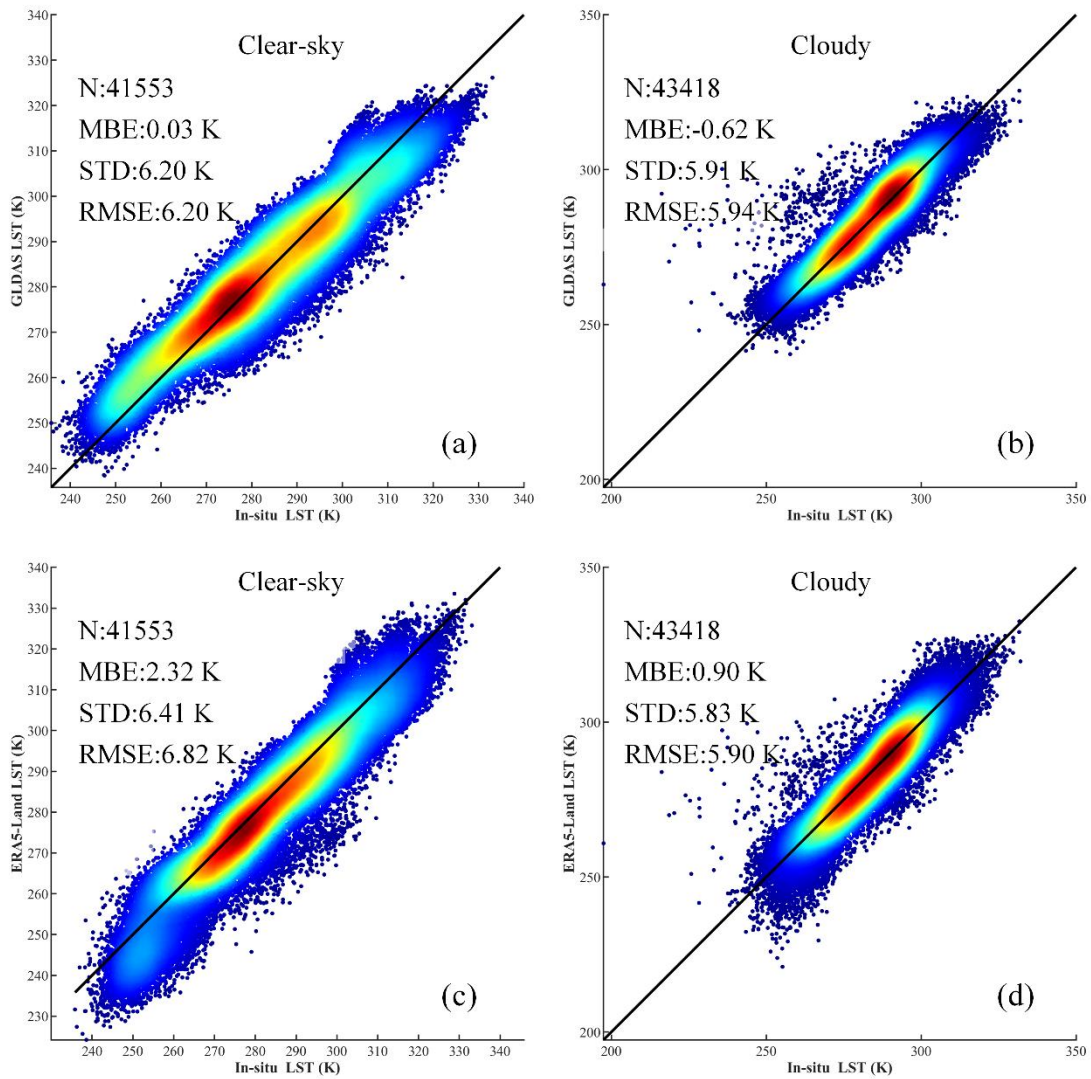
Figure 9: Density plots between reanalysis LST and *in-situ* LST.

4.4 Validation of TRIMS-Aqua LST and TRIMS-Terra LST during temporal gap

During T1 period, there are no independent *in-situ* LST measurements available. Observations of D105 and GAZ began on DOY275 (October 2) of 2002. To investigate the generalization ability of the RFSTM in the temporal dimension, the method is implemented as follows: For 2003, the GLDAS and Terra MODIS data are also merged to generate 1-km TRIMS-Terra LST. This study utilized the TSETR method to reconstruct the TRIMS-Aqua LST over a period of 915 days. To ensure a comprehensive analysis, TRIMS-Aqua LST for the years 2003 (DOY1)–2005 (DOY185) and 2013 (DOY1) – 2015 (DOY185)

491 were generated using TSETR method. This allowed for the inclusion of a significant number of independent ground sites for
492 validation purposes.
493 Table IV shows the results of the comparison between the TRIMS-Terra LST generated by the RFSTM-based method and the
494 TRIMS-Terra LST generated by the RTM-based method. The TRIMS-Terra LST generated by the RTM method and the
495 TRIMS-Terra LST generated by the RFSTM method have similar accuracies for the sites. The MBEs differ by no more than
496 0.50 K and the RMSEs differ by no more than 1.2 K. However, the RFSTM method is slightly less accurate than the TRIMS-
497 Terra LST generated by the RTM method. It is important to note that the RFSTM method is only used in this study to generate
498 data for a period of 53 days, which has a relatively smaller impact on the overall accuracy of TRIMS LST.
499
500 **Table IV: MBE and RMSE from validation results of TRIMS-Terra LST with the *in-situ* LST**

Site	Condition	TRIMS-Terra LST (RTM)				TRIMS-Terra LST (RFSTM)			
		Daytime		Nighttime		Daytime		Nighttime	
		MBE (K)	RMSE (K)	MBE (K)	RMSE (K)	MBE (K)	RMSE (K)	MBE (K)	RMSE (K)
D105	All	1.63	3.15	-1.05	1.94	1.75	3.3	-1.55	2.20
	Clear-sky	1.78	2.17	-1.17	2.04	1.85	3.34	-2.37	2.66
	Cloudy	1.54	3.25	-0.88	1.78	1.04	3.44	-0.40	1.29
GZA	All	0.93	2.61	-0.78	1.76	1.26	3.10	-1.95	2.26
	Clear-sky	0.79	2.51	-0.68	1.70	0.94	2.72	-1.26	2.10
	Cloudy	1.11	3.71	-0.94	1.85	1.61	4.20	-1.47	2.35

501
502 **Table V: MBE and RMSE from validation results of TRIMS-Aqua LST with the *in-situ* LST**

Site	Condition	TRIMS-Aqua LST (RTM)				TRIMS-Aqua LST (TSETR)			
		Daytime		Nighttime		Daytime		Nighttime	
		MBE (K)	RMSE (K)	MBE (K)	RMSE (K)	MBE (K)	RMSE (K)	MBE (K)	RMSE (K)
ARO	All	-0.53	2.14	0.58	1.77	-0.75	2.38	0.64	2.17
	Clear-sky	-0.47	2.11	0.52	1.74	-0.63	2.35	0.75	2.25
	Cloudy	-0.57	2.16	0.70	1.81	-0.87	2.34	0.88	1.85
DAM	All	-0.24	2.06	0.55	1.81	-0.38	2.47	0.60	1.84
	Clear-sky	-0.28	2.03	0.52	1.81	-0.45	2.61	0.53	2.03
	Cloudy	-0.23	2.09	0.56	1.82	-0.30	2.73	0.76	2.32
D105	All	0.80	2.67	-1.01	1.77	1.11	2.31	-1.15	1.88

25

	Clear-sky	1.55	3.05	-0.94	1.71	1.87	3.22	-1.37	1.86
	Cloudy	0.59	2.54	-1.09	1.85	0.45	1.96	-0.63	1.22
GZA	All	-0.74	2.73	-0.67	1.51	-0.93	3.01	-1.08	2.09
	Clear-sky	-0.60	2.61	-0.65	1.48	-0.98	2.74	-0.68	1.83
	Cloudy	-0.93	2.89	-0.73	1.60	-1.05	3.29	-0.94	2.24
GOB	All	-0.34	2.60	0.21	1.87	-0.62	2.77	0.47	2.15
	Clear-sky	1.88	2.41	1.64	1.93	1.77	2.76	1.66	2.04
	Cloudy	-2.31	2.75	-1.51	1.79	-2.63	2.84	-1.79	2.45
SDQ	All	-0.27	2.41	0.93	1.78	-0.59	2.75	1.23	2.40
	Clear-sky	-0.18	2.37	0.97	1.80	-0.19	2.09	1.26	2.19
	Cloudy	-0.39	2.46	0.87	1.74	-0.81	2.88	1.17	2.37

Combining the results of Table IV and Table V, it can be observed that the TRIMS-Aqua LST generated by the TSETR method and the TRIMS-Aqua LST generated by the RTM method exhibit similar accuracies at the sites. The differences in MBE and RMSE between these two methods are not significant, with the MBE differing by no more than 0.40 K and the RMSE differing by no more than 0.70 K. These findings demonstrate that the TSETR method maintains high accuracy and stability when generating data over longer time periods. Based on this, it can be concluded that the TRIMS-Aqua LST in the T1 period reconstructed using the TSETR method is reasonably accurate.

Table IV and Table V demonstrate the reliability of RFSTM and TSETR. Fig. 10 further shows the quantification results of of the similarity between the TRIMS-Aqua LST and TRIMS-Terra LST time series during the temporal gaps. Overall, the trends in the time series of TRIMS-Terra and TRIMS-Aqua LST are very consistent, and they generally have a high degree of similarity. The daytime time series show that the TRIMS-Aqua LST is generally higher than the TRIMS-Terra LST, while the opposite is observed for the nighttime. In particular, for subareas E and F, the TRIMS-Aqua LST show a significant systematic deviation from the TRIMS-Terra LST during nighttime. The distribution of the curves in Fig. 8 reveals that the daytime LST time series had more large fluctuations, while the nighttime variation is more subdued. The TSA is lower at nighttime than daytime, indicating that the time series similarity between the TRIMS-Aqua LST and the TRIMS-Terra LST is higher at nighttime. In addition, the TRIMS-Terra and TRIMS-Aqua LST are slightly more similar in the T1 than in T2 among these six regions. This situation is as expected, since the TRIMS-Aqua LST in T1 is derived from a mapping created by the data at the Terra overpass time. The differences in the TSA between T1 and T2 ranged from 0.0080 to 0.0710. The mean differences are 0.0465 (daytime) and 0.0433(nighttime). The above results indicate that the similarity of the LST time series of T1 and T2 is relatively close. This finding demonstrates that the difference between TRIMS LST at the Aqua and Terra overpass times is stable in T1.
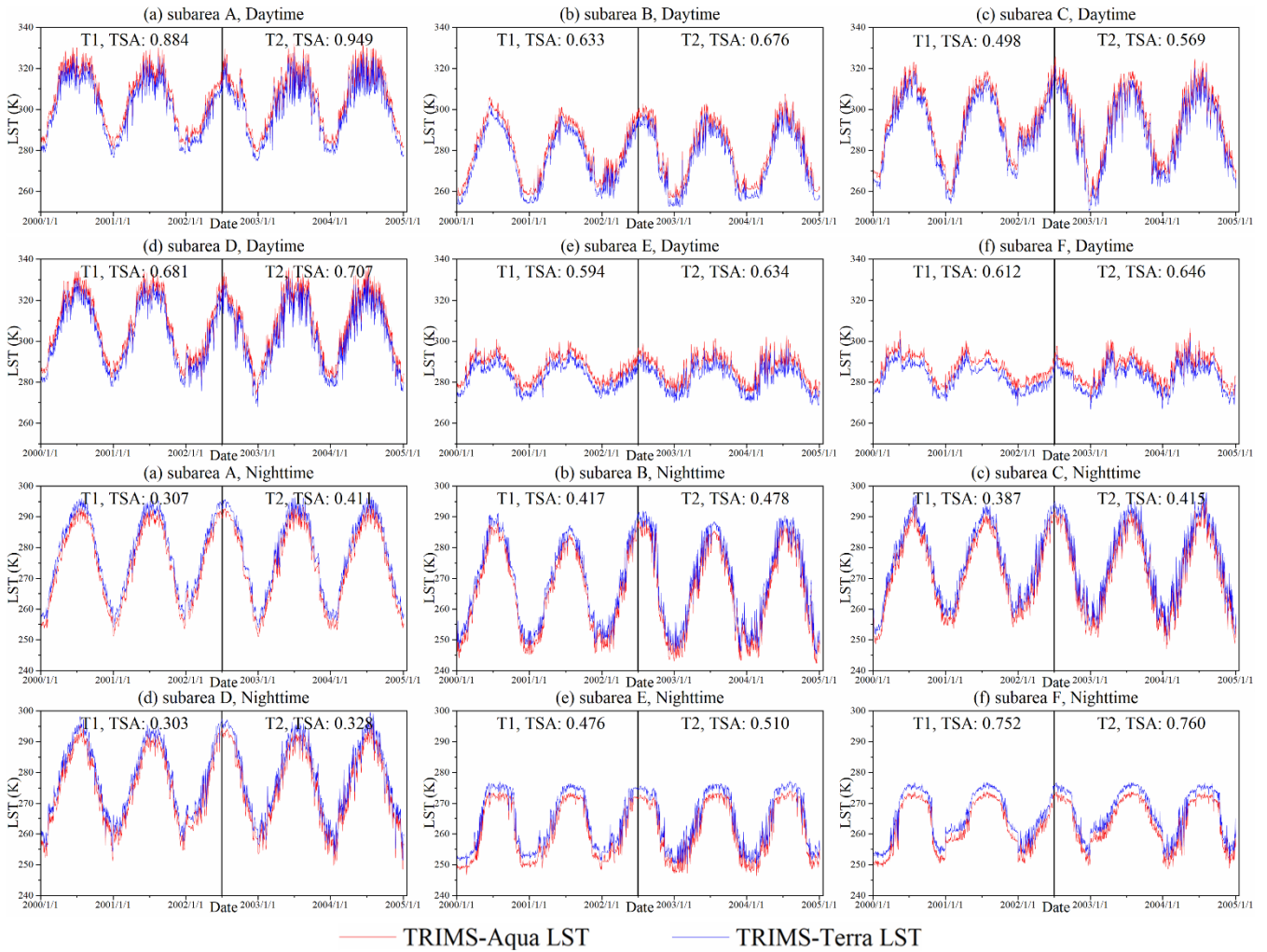
Figure 10: TRIMS-Terra and TRIMS-Aqua LSTs from January 1, 2000 to January 3, 2005 and statistics of the time series similarity.

4.5 Advantages of TRIMS LST

Recently, several all-weather LST datasets have been released by the scientific communities (see Appendix C). Overall, the uniqueness or advantages of TRIMS LST are in three main areas:

First, the TRIMS LST demonstrates comparable or better accuracy than existing publicly released all-weather/spatially seamless LST datasets. A thorough comparison with satellite TIR LST products has indicated the effectiveness of TRIMS LST, with MBD ranging from -1.5 K to 1 K and STD ranging from 1 K to 3 K, thus confirming its accuracy and consistency. Furthermore, *in-situ* LST evaluations show MBE ranging from -1.64 K to 2.88 K and RMSE ranging from 1.82 K to 3.48 K. Interestingly, no significant difference is observed between clear-sky and cloudy conditions, indicating the robustness of

27

TRIMS LST across various situations. Thus, based on the results of this study, TRIMS LST can be considered a reliable source of temperature data.

Second, the method employed in this study effectively overcomes the issue of boundary effects in reconstructing the all-weather process. This is achieved through the utilization of the E-RTM method, which is based on a temporal decomposition model of LST. With this model, the *LFC* and *HFC* components can be directly determined from high-resolution MODIS and ancillary remote sensing data. Consequently, only spatial downscaling of HFC_{cld} is required, eliminating the need for direct downscaling of the GLDAS LST. This approach reduces the possibility of insufficient spatial downscaling. Additionally, the E-RTM method considers the relationship between LSTs of neighboring pixels, resulting in decreased errors during spatial downscaling.

Third, TRIMS LST offers advantages in effectively recovering LST information and preserving temporal integrity under cloudy conditions. With a spatial resolution of 1 km, TRIMS LST covers both daytime and nighttime LST from 2000 to 2022, which is comparable in spatio-temporal resolution to other published seamless LST datasets. The E-RTM method effectively recovers temperature information under clouds, ensuring clear physical meaning and high accuracy and image quality of TRIMS LST. Moreover, TRIMS LST extends the all-weather LST coverage of the MODIS temporal gap. This enhances the completeness of long time series LST datasets, creating a unique and valuable collection.

4.6 Literature-reported applications of the TRIMS LST

TRIMS LST have already been utilized by the scientific communities in various applications (Fig. 11). A literature survey indicates that there have been 32 related papers published by journals (as of July 31, 2023), including leading journals such as Remote Sensing of Environment, Agricultural Water Management, and Science of the Total Environment. Typical applications include the estimation of soil moisture and surface evapotranspiration as well as modelling of urban heat is land and urban thermal environment. A few typical applications are listed below.
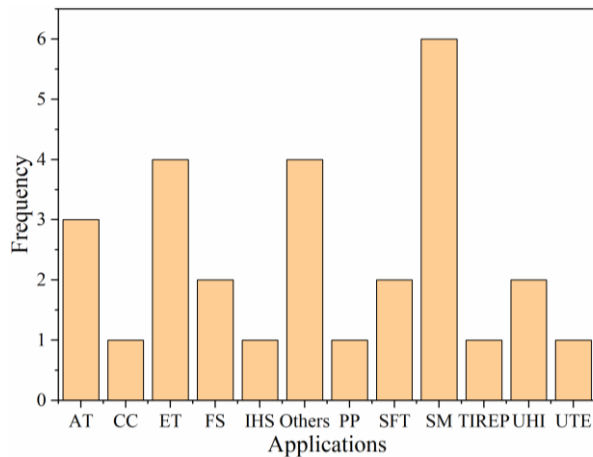
28

Satellite TIR LSTs are an important input data for obtaining SM estimates with high resolution and high spatial coverage. However, most satellite TIR LST products can only be used under clear-sky conditions. The availability of all-sky LST products provides an important opportunity to obtain SMs with spatial seamlessness. Zhang et al. (2023) combined the use of ERA5-Land and TRIMS LST for the fine-scale assessment of soil moisture in in China. They used the model based on 0.1° ERA5 Land and SM data for 1-km TRIMS LST, and finally obtained a daily/1-km SM dataset with satisfactory accuracy. Benefiting from the effective recovery of LST under cloudy conditions, this SM dataset has quasi-full spatial coverage. In addition, Hu et al. (2022) also used the TRIMS LST as input data to construct a soil moisture downscaling model for the Tibetan Plateau. The TRIMS LST was found to successfully overcome the challenges of satellite TIR remote sensing detection due to temporal/spatial gaps and false detections due to clouds and topography. Based on the downscaled soil moisture, they further published the daily 0.05°×0.05° land surface soil moisture dataset of the Qilian Mountain area (northern and northwestern Tibetan Plateau) from 2019–2021 (SMHiRes, V2) (Hu et al., 2022; Qu et al., 2021; Chai et al., 2021, 2022a, b). LST can also be used to investigate the soil freeze/thaw cycles. Li et al. (2023) used the TRIMS LST to obtain thawing degree days and freezing degree days to calculate the soil thermal conductivity and improved the output of the temperature at the top of the permafrost model. Due to the characteristics of TRIMS LST: high spatial and temporal resolution, the above two metrics can be easily obtained on a spatial scale of 1 km. In addition, the TRIMS LST was also used to evaluate the impact of the LST on the classification accuracy on different remote-sensed or model-based freeze/thaw datasets (Li et al., 2022).

Based on the TRIMS LST, Li et al. (2021b) investigated the spatial and temporal variations of surface UHI (SUHI) intensity (SUHII). The positive performance of the TRIMS LST in obtaining the LST under cloudy conditions enabled the examination of the SUHI intensity of 305 Chinese cities, especially the cities located in southern China, where clouds frequently appear. Furthermore, Liao et al. (2022) quantified the clear-sky bias of the SUHI intensity in using the MODIS LST based on the TRIMS LST. They emphasized the importance of investigating the SUHI phenomenon under cloudy conditions.

5. Data availability

TRIMS LST is available for free and easy access through the National Tibetan Plateau Data Center (TPDC): https://doi.org/10.11888/Meteoro.tpdc.271252 (Zhou et al., 2021).

6. Conclusions

A long-term 1-km daily all-weather LST dataset is the basis for supporting many applications related to land surface process and climate change. Although some all-weather LST datasets have been released, especially in the last two years, users still

589 lack such data for the period of 2000–2002, during which the MODIS LST is not available. In this study, we report a daily 1-
590 km all-weather LST dataset for the Chinese landmass and surrounding areas – TRIMS LST. In contrast to many all-weather
591 LST products, the TRIMS LST begins from the first day of the new millennium (i.e., January 1, 2000).

592 TRIMS LST is produced based on the E-RTM method. The primary input resources are the Terra/Aqua MODIS LST and
593 GLDAS LST. The TRIMS LST was comprehensively evaluated thoroughly from four aspects, including comparison with
594 satellite and reanalysis LSTs, validation against the *in-situ* LST, and similarity quantification for the TRIMS-Terra and
595 TRIMS-Aqua LST time series. The results outside the temporal gap period indicate that the TRIMS LST agrees well with the
596 original MODIS and GLDAS LST and the independent ERA5 and AATSR LST, but with more spatial details and better
597 spatio-temporal completeness. Validation of TRIMS LST using the *in-situ* LST at 19 ground sites show that the MBE was -
598 2.26 K to 1.73 K and the RMSE was 0.80 K to 3.68 K, with slightly better accuracy than the MODIS LST and no obvious
599 difference under different weather conditions. The results within the temporal gap period show that RFSTM and TSETR have
600 similar accuracy performance to the original RTM method, with MBE differences not exceeding 0.40 K and RMSE differences
601 not exceeding 0.7 K. The stability of the TRIMS LST differences for T1 at the Aqua and Terra overpass times is also a side
602 effect of the excellent quality.

603 The TRIMS LST has already been released to the scientific communities. A series of applications, such as soil moisture
604 estimation/downscaling, surface evapotranspiration estimation, and urban heat island (UHI) modelling, have been reported.
605 The TRIMS LST was found to successfully address the cloud contamination of satellite TIR LST and with good accuracy,
606 long time series, and spatio-temporal completeness. The TRIMS LST will be continuously updated to satisfy the latest
607 requirements of users.
608

Appendix A: List of abbreviations

Advanced Along-Track Scanning Radiometer	AATSR
Advanced Microwave Scanning Radiometer 2	AMSR2
30-m yearly China land cover dataset (2000-2015)	CLCD
Day of the year	DOY
the Enhanced Reanalysis and Thermal infrared remote sensing Merging method	E-RTM
Evapotranspiration	ET
Field-of-view	FOV
Goddard Earth Sciences Data and Information Services Center	GES DISC
Global Land Data Assimilation System assimilation	GLDAS
Land surface temperature	LST
Mean bias deviation	MBD
Mean bias error	MBE
MSG All-Sky Land Surface Temperature	MLST-AS
Moderate Resolution Imaging Spectroradiometer	MODIS
Normalized Difference Snow Index	NDSI
Normalized Difference Vegetation Index	NDVI
Passive microwave	PMW
Random-Forest based Spatio-Temporal Merging approach	RFSTM
Root mean square error	RMSE
Soil moisture	SM
'Satellite Pour l'Observation de la Terre' (SPOT) VEGETATION (VGT)	SPOT VGT
Shuttle Radar Topography Mission Digital Elevation Model data	SRTM DEM
Standard deviation	STD
Surface UHI	SUHI
Surface UHI intensity	SUHII
Thermal infrared remote sensing	TIR
the National Tibetan Plateau Data Center	TPDC
the Thermal and Reanalysis Integrating Moderate-resolution Spatial- seamless LST	TRIMS LST
Time series angle	TSA
Time-SEquential LST based Reconstruction approach	TSETR
Urban heat island	UHI
Visible infrared Imaging Radiometer	VIIRS

610

Appendix B: Validation results of the TRIMS LST and the MODIS LST with the *in-situ* LST

Table B1: MBE and RMSE from validation results of the daytime TRIMS LST and MODIS LST with *in-situ* LST

Site	Condition	Sample size		TRIMS LST				MODIS LST			
				MBE (K)		RMSE (K)		MBE (K)		RMSE (K)	
		MOD	MYD	MOD	MYD	MOD	MYD	MOD	MYD	MOD	MYD
ARO	Clear-sky	1418	1029	0.43	0.48	2.30	1.87	0.74	0.57	2.95	2.38
	Cloudy	1228	1541	0.33	0.61	2.04	1.95	–	–	–	–
DAM	Clear-sky	1363	1297	0.97	0.26	1.92	1.98	0.98	0.27	2.31	2.50
	Cloudy	1432	1492	0.67	0.18	1.81	2.07	–	–	–	–
DET	Clear-sky	1191	1180	1.73	1.45	2.45	2.49	1.73	1.88	2.70	2.70
	Cloudy	830	896	1.70	1.45	2.67	2.43	–	–	–	–
DSL	Clear-sky	1109	814	-0.01	-0.33	1.82	1.72	0.00	-0.32	2.38	2.28
	Cloudy	1198	1144	-0.01	0.48	1.91	1.65	–	–	–	–
EBA	Clear-sky	410	289	0.63	0.59	2.06	1.90	0.65	0.53	2.38	2.31
	Cloudy	472	580	0.74	0.61	2.01	1.80	–	–	–	–
GOB	Clear-sky	363	350	-0.58	-1.88	1.73	2.41	-0.61	-1.89	2.25	2.74
	Cloudy	368	390	-0.96	-1.65	1.72	2.71	–	–	–	–
HZZ	Clear-sky	1046	975	1.06	-1.03	1.84	2.06	1.05	-1.04	2.40	3.14
	Cloudy	1219	1354	0.59	-0.66	1.78	2.05	–	–	–	–
SDQ	Clear-sky	1507	1466	0.82	0.23	2.57	2.05	0.81	0.39	3.16	2.57
	Cloudy	1147	1132	0.86	0.37	2.49	2.23	–	–	–	–
SSW	Clear-sky	191	174	-0.42	-1.33	2.09	2.08	-0.43	-1.35	3.10	2.51
	Cloudy	194	203	-1.23	-1.77	2.36	2.45	–	–	–	–
HLA	Clear-sky	1121	946	-0.79	-0.85	2.30	2.18	-0.74	-0.71	2.76	2.60
	Cloudy	1084	1159	-0.68	-0.75	2.68	1.81	–	–	–	–
D105	Clear-sky	92	44	1.61	1.28	3.68	2.53	1.36	0.67	4.09	2.71
	Cloudy	178	138	1.29	0.61	3.94	2.74	–	–	–	–
GAZ	Clear-sky	220	240	0.74	-0.60	2.12	2.17	0.47	-0.55	2.37	2.82

Site	Condition	MOD	MYD	MOD	MYD	MOD	MYD	MOD	MYD	MOD	MYD
	Cloudy	89	157	1.15	-0.85	2.11	1.96	–	–	–	–
CBS	Clear-sky	54	56	0.49	1.38	2.41	3.41	0.85	1.49	2.39	3.43
	Cloudy	220	262	0.76	1.59	2.42	3.43	–	–	–	–
DXI	Clear-sky	246	226	0.83	0.30	2.13	1.79	0.80	0.28	2.33	2.00
	Cloudy	547	562	0.81	0.54	2.19	1.79	–	–	–	–
DHS	Clear-sky	23	21	0.38	0.77	1.37	1.53	0.30	0.74	0.74	1.18
	Cloudy	292	299	0.42	0.47	1.51	1.22	–	–	–	–
MQU	Clear-sky	101	64	0.15	-1.50	2.43	2.85	0.12	-1.47	3.05	3.13
	Cloudy	77	117	0.05	-1.35	2.27	2.99	–	–	–	–
GUT	Clear-sky	69	63	-0.22	0.02	2.10	2.25	-0.29	-0.07	2.20	2.25
	Cloudy	310	303	-0.28	0.60	1.83	2.22	–	–	–	–
QYZ	Clear-sky	26	19	0.95	1.01	3.00	3.17	0.73	0.90	2.35	2.14
	Cloudy	139	177	0.71	0.91	2.71	3.35	–	–	–	–
TYU	Clear-sky	211	196	0.37	-0.88	2.56	2.14	0.31	-0.90	3.01	2.63
	Cloudy	333	348	0.19	-0.58	2.63	2.03	–	–	–	–

Table B2: MBE and RMSE from validation results of the nighttime TRIMS LST and MODIS LST with the *in-situ* LST.

Site	Condition	Sample size		TRIMS LST				MODIS LST			
				MBE (K)		RMSE (K)		MBE (K)		RMSE (K)	
		MOD	MYD	MOD	MYD	MOD	MYD	MOD	MYD	MOD	MYD
ARO	Clear-sky	1617	1757	-0.72	-0.53	1.87	1.67	-0.70	-0.60	2.09	1.90
	Cloudy	1196	1078	-0.68	-0.63	1.62	1.76	–	–	–	–
DAM	Clear-sky	853	973	-0.80	-0.58	2.14	1.70	-0.82	-0.81	2.23	1.87
	Cloudy	1643	1673	-0.86	-0.52	1.98	1.64	–	–	–	–
DET	Clear-sky	1325	1476	-0.08	0.17	0.83	0.90	-0.08	0.16	0.86	0.97
	Cloudy	679	630	0.42	-0.23	0.80	0.83	–	–	–	–
DSL	Clear-sky	1109	1646	-0.90	-0.84	1.82	1.50	-0.45	-0.42	1.92	1.78
	Cloudy	1198	797	-1.13	0.44	1.91	1.24	–	–	–	–
EBA	Clear-sky	566	621	-0.61	-0.60	1.65	2.00	-0.58	-0.64	1.77	2.19
	Cloudy	443	404	-0.55	-0.64	1.56	1.68	–	–	–	–

GOB	Clear-sky	467	381	-1.60	-1.65	2.05	1.93	-1.62	-1.65	1.96	1.96
	Cloudy	376	321	-2.04	-1.51	2.26	1.79	–	–	–	–
HZZ	Clear-sky	772	944	-1.29	-0.94	1.86	1.46	-1.28	-0.93	2.03	1.65
	Cloudy	1348	1296	-1.77	-1.36	2.32	1.86	–	–	–	–
SDQ	Clear-sky	1557	1286	-0.79	-0.94	2.61	2.33	-1.02	-0.93	2.68	2.44
	Cloudy	1112	981	-1.06	-0.94	2.70	2.15	–	–	–	–
SSW	Clear-sky	172	164	-2.26	-1.87	2.53	2.11	-2.27	-1.86	2.59	2.15
	Cloudy	195	190	-1.95	-1.79	2.29	2.00	–	–	–	–
HLA	Clear-sky	1042	1038	-0.82	-0.73	2.24	1.61	-0.85	-0.73	2.34	1.75
	Cloudy	1066	989	-0.85	-0.87	2.24	1.55	–	–	–	–
D105	Clear-sky	131	167	-1.07	-0.92	2.39	2.57	-1.05	-1.12	2.58	2.69
	Cloudy	95	121	-1.05	-1.10	2.81	2.74	–	–	–	–
GAZ	Clear-sky	289	265	-0.63	-0.68	1.85	1.35	-0.68	-0.57	1.90	1.39
	Cloudy	124	86	-0.75	-0.69	1.80	1.32	–	–	–	–
CBS	Clear-sky	95	98	-1.07	-0.55	2.81	2.21	-1.00	-0.50	2.79	2.26
	Cloudy	190	208	-1.00	-0.33	3.31	2.37	–	–	–	–
DXI	Clear-sky	334	349	-1.10	-1.45	3.43	3.06	-1.65	-1.44	3.51	3.13
	Cloudy	454	446	-1.15	-1.42	3.77	2.58	–	–	–	–
DHS	Clear-sky	53	53	-0.82	-0.74	1.97	2.31	-0.74	-0.89	1.83	2.22
	Cloudy	264	262	-0.81	-0.89	2.35	2.30	–	–	–	–
MQU	Clear-sky	85	81	0.68	0.78	2.23	2.41	0.76	0.70	2.16	2.40
	Cloudy	105	90	0.81	0.76	2.32	2.53	–	–	–	–
GUT	Clear-sky	122	126	-0.90	-0.76	2.14	1.80	-0.94	-0.78	2.19	1.81
	Cloudy	237	230	-0.93	-0.70	2.49	1.78	–	–	–	–
QYZ	Clear-sky	32	28	-0.90	-0.91	3.00	2.09	-1.16	-0.80	2.62	1.88
	Cloudy	145	175	-1.13	-0.88	3.49	2.37	–	–	–	–
TYU	Clear-sky	235	242	-1.12	-0.78	2.65	2.26	-0.94	-0.75	2.69	2.25
	Cloudy	258	273	-1.13	-0.79	2.91	2.37	–	–	–	–

Appendix C: Summary of publicly available all-weather/all-sky/gap-free LST products.

Product	Spatial resolution	Temporal resolution	Spatial coverage	Temporal coverage	Download links	References
All-weather 1 km land surface temperature products for China	1 km	1 observation per day	China	2002-2011	http://www.geodata.cn /index.html	Duan et al.（2017）
Global monthly reconstructed minimum, average, and maximum LST data (2003－2016)	5.6 km	Monthly Mean	Global	2003-2016	http://doi.org/10.5281/ zenodo.1115666	Metz et al. (2017)
Daily 1-km all-weather land surface temperature dataset for Western China V1	1 km	2 observations per day	65.00°-108°E, 45.00°-22°N	2003-2018	https://data.tpdc.ac.cn (Expired)	Zhang et al.(2019b, 2020a)
MSG Land Surface Temperature - All Sky (MLST-AS) (LSA-005)	3-5 km	15 min	Europe and Africa	2020-Now	https://landsaf.ipma.pt/ en	Martins et al. (2019)
1 km seamless land surface temperature dataset of China (2002-2020) (2002－2020)	1 km	2 observations per day	China	2002-2020	https://data.tpdc.ac.cn	Xu and Cheng. (2021); Zhang and Cheng. (2020b); Zhang et al. (2020c)
A combined Terra and Aqua MODIS land surface temperature and meteorological station data product for China (2003－2017)	5.6 km	Monthly Mean	China	2003-2017	https://data.tpdc.ac.cn	Zhao et al. (2020a)
Daily 1-km all-weather land surface temperature dataset for Western China (TRIMS LST-TP; 2000－2022) V2	1 km	4 observations per day	72.00°-104°E, 45.00°-20°N	2000-2022	https://data.tpdc.ac.cn	Zhang et al. (2021)
Daily 1-km all-weather land surface temperature dataset for the Chinese landmass and its surrounding areas (TRIMS LST; 2000－2022)	1 km	4 observations per day	72.00°-135°E, 19.00°-55°N	2000-2022	https://data.tpdc.ac.cn	Zhang et al. (2021)

Worldwide continuous gap-filled MODIS land surface temperature dataset	1 km	2 observations per day	Global	2002-Now	https://shilosh.users.earthengine.app/view/continuous-lst	Shiff et al. (2021)
Global daily 0.05°spatiotemporal continuous land surface temperature dataset (2002–2020)	0.05°	4 observations per day	Global	2002-2020	https://data.tpdc.ac.cn	Yu et al. (2022)
A global seamless 1 km resolution daily land surface temperature dataset (2003–2020)	1 km	2 observations per day	Global	2003-2020	https://doi.org/10.25380/iastate.c.5078492	Zhang et al. (2022)
Global spatiotemporally seamless T$_{dm}$ products ranging from 2003 to 2019 (GADTC products)	0.5°	Daily mean	Global	2003-2019	https://doi.org/10.5281/zenodo.6287052	Hong et al. (2022)
0.02° seamless hourly land surface temperature dataset over East Asia (2016–2021)	0.02°	Hourly	East Asia	2016-2021	http://data.tpdc.ac.cn/zh-hans/data/06414391-abd4-4d28-a844-bd036a0b8c55/	Dong et al. (2022); Zhou and Cheng. (2020)
Global Hourly, 5-km, All-sky Land Surface Temperature (GHA-LST)	5 km	Hourly	Global	2011-2021	https://doi.org/10.5281/zenodo.6981704; glass.umd.edu/allsky_LST/GHA-LST	Jia et al. (2022)
Daily 1km all-sky time-consistent land surface temperature dataset over the Tibetan Plateau （2001–2018）	1 km	Daily	Qinghai Tibet Plateau	2001-2018	https://data.tpdc.ac.cn/zh-hans/data/3eb11507-6742-4f16-bda2-8ea10e0c1606	Zhao. (2023)
Global seamless and high-resolution temperature dataset (GSHTD)	1 km	Monthly Mean	Global	2001-2020	https://cjgeodata.cug.edu.cn/#/pageDetail?id=97	Yao et al. (2023)

Author contribution

620   WBT implemented the E-RTM method, completed the thorough evaluation and wrote the earliest version of the manuscript, JZ examined the entire process of generation and release of the TRIMS LST dataset and provided necessary guidance, JM helped to obtain the measured data and provided the method to quantify the spatial representation, and XDZ and JZ proposed the original RTM method. All co-authors contributed to the writing and carefully reviewed and revised the manuscript.

Competing interests

625   The authors declare that they have no conflict of interest.

References

Aguilar-Lome, J., Espinoza-Villar, R., Espinoza, J.-C., Rojas-Acuna, J., Leo Willems, B., and Leyva-Molina, W.-M.: Elevation-dependent warming of land surface temperatures in the Andes assessed using MODIS LST time series (2000-2017), Int. J. Appl. Earth Obs. Geoinformation, 77, 119–128, https://doi.org/10.1016/j.jag.2018.12.013, 2019.

640   Alexander, C.: Normalised difference spectral indices and urban land cover as indicators of land surface temperature (LST), Int. J. Appl. Earth Obs. Geoinformation, 86, 102013, https://doi.org/10.1016/j.jag.2019.102013, 2020.

Anderson, M. C., Kustas, W. P., Norman, J. M., Hain, C. R., Mecikalski, J. R., Schultz, L., González-Dugo, M. P., Cammalleri, C., d'Urso, G., Pimstein, A., and Gao, F.: Mapping daily evapotranspiration at field to continental scales using geostationary and polar orbiting satellite imagery, Hydrol. Earth Syst. Sci., 15, 223–239, https://doi.org/10.5194/hess-15-223-2011, 2011.

645   Bechtel, B.: A New Global Climatology of Annual Land Surface Temperature, Remote Sens., 7, 2850–2870, https://doi.org/10.3390/rs70302850, 2015.

Breiman, L.: Random Forests, Machine Learning, 45, 5–32, https://doi.org/10.1023/A:1010933404324, 2001.

Chai, L., Zhu, Z., and Liu, S.: Daily 0.05°×0.05° land surface soil moisture dataset of Qilian Mountain area (2019,SMHiRes,V2), edited by: National Tibetan Plateau Data Center, Natl. Tibet. Plateau Data Cent., 2021.

650 Chai, L., Zhu, Z., and Liu, S.: Daily 0.05°×0.05° land surface soil moisture dataset of Qilian Mountain area (2020,SMHiRes,V2), edited by: National Tibetan Plateau Data Center, Natl. Tibet. Plateau Data Cent., https://doi.org/10.11888/Terre.tpdc.272375, 2022a.

Chai, L., Zhu, Z., and Liu, S.: Daily 0.05°×0.05° land surface soil moisture dataset of Qilian Mountain area (2021,SMHiRes,V2), edited by: National Tibetan Plateau Data Center, Natl. Tibet. Plateau Data Cent., 655 https://doi.org/10.11888/Terre.tpdc.272375, 2022b.

Che, T., Li, X., Liu, S., Li, H., Xu, Z., Tan, J., Zhang, Y., Ren, Z., Xiao, L., Deng, J., Jin, R., Ma, M., Wang, J., and Yang, X.: Integrated hydrometeorological, snow and frozen-ground observations in the alpine region of the Heihe River Basin, China, Earth Syst. Sci. Data, 11, 1483–1499, https://doi.org/10.5194/essd-11-1483-2019, 2019.

Chen, C., Park, T., Wang, X., Piao, S., Xu, B., Chaturvedi, R. K., Fuchs, R., Brovkin, V., Ciais, P., Fensholt, R., Tømmervik, 660 H., Bala, G., Zhu, Z., Nemani, R. R., and Myneni, R. B.: China and India lead in greening of the world through land-use management, Nat. Sustain., 2, 122–129, https://doi.org/10.1038/s41893-019-0220-7, 2019a.

Chen, S., Chen, X., Chen, W., Su, Y., and Li, D.: A simple retrieval method of land surface temperature from AMSR-E passive microwave data—A case study over Southern China during the strong snow disaster of 2008, Int. J. Appl. Earth Obs. Geoinformation, 13, 140–151, 2011.

665 Chen, Y., Chen, W., Su, Q., Luo, F., Sparrow, S., Wallom, D., Tian, F., Dong, B., Tett, S. F. B., and Lott, F. C.: Anthropogenic Warming has Substantially Increased the Likelihood of July 2017–Like Heat Waves over Central Eastern China, Bull. Am. Meteorol. Soc., 100, S91–S95, https://doi.org/10.1175/BAMS-D-18-0087.1, 2019b.

Coops, N. C., Duro, D. C., Wulder, M. A., and Han, T.: Estimating afternoon MODIS land surface temperatures (LST) based on morning MODIS overpass, location and elevation information, Int. J. Remote Sens., 28, 2391–2396, 670 https://doi.org/10.1080/01431160701294653, 2007.

Ding, L., Zhou, J., Li, Z.-L., Ma, J., Shi, C., Sun, S., and Wang, Z.: Reconstruction of Hourly All-Weather Land Surface Temperature by Integrating Reanalysis Data and Thermal Infrared Data From Geostationary Satellites (RTG), IEEE Trans. Geosci. Remote Sens., 60, 1–17, https://doi.org/10.1109/TGRS.2022.3227074, 2022.

Ding, L., Zhou J., Zhang X., Wang S., Tang W., Wang Z., Ma J., Ai L., Li M.,and Wang W.: Estimation of all-weather land 675 surface temperature with remote sensing: Progress and challenges, National Remote Sensing Bulletin., 27(7):1534-1553, https://doi.org/10.11834/jrs.20211323, 2023.

Dong, S., Cheng, J., Shi, J., Shi, C., Sun, S., and Liu, W.: A Data Fusion Method for Generating Hourly Seamless Land Surface Temperature from Himawari-8 AHI Data, Remote Sensing, 14, 5170, https://doi.org/10.3390/rs14205170, 2022.

Duan, S., Li, Z., and Leng, P.: A framework for the retrieval of all-weather land surface temperature at a high spatial resolution 680 from polar-orbiting thermal infrared and passive microwave data, Remote Sens. Environ., 195, 107–117, https://doi.org/10.1016/j.rse.2017.04.008, 2017.

Freitas, S. C., Trigo, I. F., Bioucas-Dias, J. M., and Gottsche, F.-M.: Quantifying the Uncertainty of Land Surface Temperature Retrievals From SEVIRI/Meteosat, IEEE Trans. Geosci. Remote Sens., 48, 523–534, https://doi.org/10.1109/TGRS.2009.2027697, 2010.

685   Feng, Y., Liu, Q., Qu, Y., and Liang, S.: Estimation of the Ocean Water Albedo From Remote Sensing and Meteorological Reanalysis Data, IEEE Transactions on Geoscience and Remote Sensing, 54, 850–868, https://doi.org/10.1109/TGRS.2015.2468054, 2016.

Fu, B., Li, S., Yu, X., Yang, P., Yu, G., Feng, R., and Zhuang, X.: Chinese ecosystem research network: Progress and perspectives, Ecological Complexity, 7, 225–233, https://doi.org/10.1016/j.ecocom.2010.02.007, 2010.

690   Göttsche, F.-M., Olesen, F.-S., Trigo, I. F., Bork-Unkelbach, A., and Martin, M. A.: Long Term Validation of Land Surface Temperature Retrieved from MSG/SEVIRI with Continuous in-Situ Measurements in Africa, Remote Sens., 8, 410, https://doi.org/10.3390/rs8050410, 2016.

Guo, A., Liu, S., Zhu, Z., Xu, Z., Xiao, Q., Ju, Q., Zhang, Y., and Yang, X.: Impact of Lake/Reservoir Expansion and Shrinkage on Energy and Water Vapor Fluxes in the Surrounding Area, J. Geophys. Res.-Atmospheres, 125, e2020JD032833,
695   https://doi.org/10.1029/2020JD032833, 2020.

Holmes, T. R. H., De Jeu, R. a. M., Owe, M., and Dolman, A. J.: Land surface temperature from Ka band (37 GHz) passive microwave observations, J. Geophys. Res. Atmospheres, 114, https://doi.org/10.1029/2008JD010257, 2009.

Hong, F., Zhan, W., Göttsche, F.-M., Liu, Z., Dong, P., Fu, H., Huang, F., and Zhang, X.: A global dataset of spatiotemporally seamless daily mean land surface temperatures: generation, validation, and analysis, Earth Syst. Sci. Data, 14, 3091–3113,
700   https://doi.org/10.5194/essd-14-3091-2022, 2022.

Hu, Z., Chai, L., Crow, W. T., Liu, S., Zhu, Z., Zhou, J., Qu, Y., Liu, J., Yang, S., and Lu, Z.: Applying a Wavelet Transform Technique to Optimize General Fitting Models for SM Analysis: A Case Study in Downscaling over the Qinghai-Tibet Plateau, Remote Sens., 14, 3063, https://doi.org/10.3390/rs14133063, 2022.

Jia, A., Ma, H., Liang, S., and Wang, D.: Cloudy-sky land surface temperature from VIIRS and MODIS satellite data using a
705   surface energy balance-based method, Remote Sens. Environ., 263, 112566, https://doi.org/10.1016/j.rse.2021.112566, 2021.

Jia, A., Liang, S., Wang, D., Ma, L., Wang, Z., and Xu, S.: Global hourly, 5 km, all-sky land surface temperature data from 2011 to 2021 based on integrating geostationary and polar-orbiting satellite data, Earth Syst. Sci. Data Discuss., 1–35, https://doi.org/10.5194/essd-2022-284, 2022.

Jiang, G.-M. and Liu, R.: Retrieval of Sea and Land Surface Temperature From SVISSR/FY-2C/D/E Measurements, IEEE
710   Trans. Geosci. Remote Sens., 52, 6132–6140, https://doi.org/10.1109/TGRS.2013.2295260, 2014.

Jin, M. and Dickinson, R. E.: A generalized algorithm for retrieving cloudy sky skin temperature from satellite thermal infrared radiances, J. Geophys. Res. Atmospheres, 105, 27037–27047, https://doi.org/10.1029/2000JD900318, 2000.

Kruse, F., Lefkoff, A., Boardman, J., Heidebrecht, K., Shapiro, A., Barloon, P., and Goetz, A.: The Spectral Image-Processing System (sips) - Interactive Visualization and Analysis of Imaging Spectrometer Data, Remote Sens. Environ., 44, 145–163,
715   https://doi.org/10.1016/0034-4257(93)90013-N, 1993.

Li, B., Liang, S., Liu, X., Ma, H., Chen, Y., Liang, T., and He, T.: Estimation of all-sky 1 km land surface temperature over the conterminous United States, Remote Sens. Environ., 266, 112707, https://doi.org/10.1016/j.rse.2021.112707, 2021a.

Li, H., Chai, L., Crow, W., Dong, J., Liu, S., and Zhao, S.: The reliability of categorical triple collocation for evaluating soil freeze/ thaw datasets, REMOTE Sens. Environ., 281, https://doi.org/10.1016/j.rse.2022.113240, 2022.

720 Li, K., Chen, Y., and Gao, S.: Comparative Analysis of Variations and Patterns between Surface Urban Heat Island Intensity and Frequency across 305 Chinese Cities, Remote Sens., 13, 3505, https://doi.org/10.3390/rs13173505, 2021b.

Li, W., Weng, B., Yan, D., Lai, Y., Li, M., and Wang, H.: Underestimated permafrost degradation: Improving the TTOP model based on soil thermal conductivity, Sci. TOTAL Environ., 854, https://doi.org/10.1016/j.scitotenv.2022.158564, 2023a.

Li, X., Cheng, G., Liu, S., Xiao, Q., Ma, M., Jin, R., Che, T., Liu, Q., Wang, W., Qi, Y., Wen, J., Li, H., Zhu, G., Guo, J., Ran,
725 Y., Wang, S., Zhu, Z., Zhou, J., Hu, X., and Xu, Z.: Heihe Watershed Allied Telemetry Experimental Research (HiWATER): Scientific Objectives and Experimental Design, Bull. Am. Meteorol. Soc., 94, 1145–1160, https://doi.org/10.1175/BAMS-D-12-00154.1, 2013a.

Li, X., Zhou, Y., Asrar, G. R., and Zhu, Z.: Creating a seamless 1km resolution daily land surface temperature dataset for urban and surrounding areas in the conterminous United States, Remote Sens. Environ., 206, 84–97,
730 https://doi.org/10.1016/j.rse.2017.12.010, 2018.

Li, Y., Li, Z.-L., Wu, H., Zhou, C., Liu, X., Leng, P., Yang, P., Wu, W., Tang, R., Shang, G.-F., and Ma, L.: Biophysical impacts of earth greening can substantially mitigate regional land surface temperature warming, Nat Commun, 14, 121, https://doi.org/10.1038/s41467-023-35799-4, 2023b.

Li, Z.-L., Tang, B.-H., Wu, H., Ren, H., Yan, G., Wan, Z., Trigo, I. F., and Sobrino, J. A.: Satellite-derived land surface
735 temperature: Current status and perspectives, Remote Sens. Environ., 131, 14–37, https://doi.org/10.1016/j.rse.2012.12.008, 2013b.

Li, Z.-L., Wu, H., Duan, S.-B., Zhao, W., Ren, H., Liu, X., Leng, P., Tang, R., Ye, X., Zhu, J., Sun, Y., Si, M., Liu, M., Li, J., Zhang, X., Shang, G., Tang, B.-H., Yan, G., and Zhou, C.: Satellite Remote Sensing of Global Land Surface Temperature: Definition, Methods, Products, and Applications, Rev. Geophys., 61, e2022RG000777,
740 https://doi.org/10.1029/2022RG000777, 2023c.

Liao, Y., Shen, X., Zhou, J., Ma, J., Zhang, X., Tang, W., Chen, Y., Ding, L., and Wang, Z.: Surface urban heat island detected by all-weather satellite land surface temperature, Sci. Total Environ., 811, 151405, https://doi.org/10.1016/j.scitotenv.2021.151405, 2022.

Liu, H., Dong, W., Fu, C., and Beijing: The Long-Term Field Experiment on Aridification and the Ordered HumanActivity in
745 Semi-Arid Area at Tongyu, Northeast China, Clim. Environ. Res., 2004.

Liu, N. F., Liu, Q., Wang, L. Z., Liang, S. L., Wen, J. G., Qu, Y., and Liu, S. H.: A statistics-based temporal filter algorithm to map spatiotemporally continuous shortwave albedo from MODIS data, Hydrology and Earth System Sciences, 17, 2121–2129, https://doi.org/10.5194/hess-17-2121-2013, 2013a.

Liu, S., Li, X., Xu, Z., Che, T., Xiao, Q., Ma, M., Liu, Q., Jin, R., Guo, J., Wang, L., Wang, W., Qi, Y., Li, H., Xu, T., Ran,
750 Y., Hu, X., Shi, S., Zhu, Z., Tan, J., Zhang, Y., and Ren, Z.: The Heihe Integrated Observatory Network: A Basin-Scale Land Surface Processes Observatory in China, Vadose Zone J., 17, 180072, https://doi.org/10.2136/vzj2018.04.0072, 2018.

Liu, S. M., Xu, Z. W., Wang, W. Z., Jia, Z. Z., Zhu, M. J., Bai, J., and Wang, J. M.: A comparison of eddy-covariance and large aperture scintillometer measurements with respect to the energy balance closure problem, Hydrol. Earth Syst. Sci., 15, 1291–1306, https://doi.org/10.5194/hess-15-1291-2011, 2011.

Liu, S. M., Xu, Z. W., Zhu, Z. L., Jia, Z. Z., and Zhu, M. J.: Measurements of evapotranspiration from eddy-covariance systems and large aperture scintillometers in the Hai River Basin, China, J. Hydrol., 487, 24–38, https://doi.org/10.1016/j.jhydrol.2013.02.025, 2013b.

Liu, Y., Hiyama, T., and Yamaguchi, Y.: Scaling of land surface temperature using satellite data: A case examination on ASTER and MODIS products over a heterogeneous terrain area, Remote Sens. Environ., 105, 115–128, https://doi.org/10.1016/j.rse.2006.06.012, 2006.

Long, D., Yan, L., Bai, L., Zhang, C., Li, X., Lei, H., Yang, H., Tian, F., Zeng, C., Meng, X., and Shi, C.: Generation of MODIS-like land surface temperatures under all-weather conditions based on a data fusion approach, Remote Sens. Environ., 246, 111863, https://doi.org/10.1016/j.rse.2020.111863, 2020.

Ma, J., Zhou, J., Göttsche, F.-M., Wang, Z., Wu, H., Tang, W., Li, M., and Liu, S.: An atmospheric influence correction method for longwave radiation-based in-situ land surface temperature, Remote Sensing of Environment, 293, 113611, https://doi.org/10.1016/j.rse.2023.113611, 2023.

Ma, J., Zhou, J., Liu, S., Göttsche, F.-M., Zhang, X., Wang, S., and Li, M.: Continuous evaluation of the spatial representativeness of land surface temperature validation sites, Remote Sens. Environ., 265, 112669, https://doi.org/10.1016/j.rse.2021.112669, 2021.

Ma, Y., Yao, T., and Wang, J.: Experimental study of energy and water cycle in Tibetan Plateau: The progress introduction on the study of GAME/Tibet and CAMP/Tibet, Plateau Meteorol., 25, 344–351, 2006.

Ma, Y., Zhou, J., Liu, S., Zhang, W., Zhang, Y., Xu, Z., Song, L., and Zhao, H.: Estimation of evapotranspiration using all-weather land surface temperature and variational trends with warming temperatures for the River Source Region in Southwest China, J. Hydrol., 613, 128346, https://doi.org/10.1016/j.jhydrol.2022.128346, 2022.

Martins, J. P. A., Trigo, I. F., Ghilain, N., Jimenez, C., Göttsche, F.-M., Ermida, S. L., Olesen, F.-S., Gellens-Meulenberghs, F., and Arboleda, A.: An All-Weather Land Surface Temperature Product Based on MSG/SEVIRI Observations, Remote Sens., 11, 3044, https://doi.org/10.3390/rs11243044, 2019.

Metz, M., Andreo, V., and Neteler, M.: A New Fully Gap-Free Time Series of Land Surface Temperature from MODIS LST Data, Remote Sens., 9, 1333, https://doi.org/10.3390/rs9121333, 2017.

Mildrexler, D. J., Zhao, M., Cohen, W. B., Running, S. W., Song, X. P., and Jones, M. O.: Thermal Anomalies Detect Critical Global Land Surface Changes, J. Appl. Meteorol. Climatol., 57, 391–411, 2018.

Muñoz-Sabater, J., Dutra, E., Agustí-Panareda, A., Albergel, C., Arduini, G., Balsamo, G., Boussetta, S., Choulga, M., Harrigan, S., Hersbach, H., Martens, B., Miralles, D. G., Piles, M., Rodríguez-Fernández, N. J., Zsoter, E., Buontempo, C., and Thépaut, J.-N.: ERA5-Land: a state-of-the-art global reanalysis dataset for land applications, Earth Syst. Sci. Data, 13, 4349–4383, https://doi.org/10.5194/essd-13-4349-2021, 2021.

Parinussa, R., Lakshmi, V., Johnson, F., and Sharma, A.: Comparing and Combining Remotely Sensed Land Surface Temperature Products for Improved Hydrological Applications, Remote Sens., 8, 162, https://doi.org/10.3390/rs8020162, 2016.

Pastorello, G., Trotta, C., Canfora, E., Chu, H., Christianson, D., Cheah, Y.-W., Poindexter, C., Chen, J., Elbashandy, A., Humphrey, M., Isaac, P., Polidori, D., Reichstein, M., Ribeca, A., van Ingen, C., Vuichard, N., Zhang, L., Amiro, B., Ammann, C., Arain, M. A., Ardö, J., Arkebauer, T., Arndt, S. K., Arriga, N., Aubinet, M., Aurela, M., Baldocchi, D., Barr, A., Beamesderfer, E., Marchesini, L. B., Bergeron, O., Beringer, J., Bernhofer, C., Berveiller, D., Billesbach, D., Black, T. A.,

Blanken, P. D., Bohrer, G., Boike, J., Bolstad, P. V., Bonal, D., Bonnefond, J.-M., Bowling, D. R., Bracho, R., Brodeur, J., Brümmer, C., Buchmann, N., Burban, B., Burns, S. P., Buysse, P., Cale, P., Cavagna, M., Cellier, P., Chen, S., Chini, I., Christensen, T. R., Cleverly, J., Collalti, A., Consalvo, C., Cook, B. D., Cook, D., Coursolle, C., Cremonese, E., Curtis, P. S., D'Andrea, E., da Rocha, H., Dai, X., Davis, K. J., Cinti, B. D., Grandcourt, A. de, Ligne, A. D., De Oliveira, R. C., Delpierre, N., Desai, A. R., Di Bella, C. M., Tommasi, P. di, Dolman, H., Domingo, F., Dong, G., Dore, S., Duce, P., Dufrêne, E., Dunn, A., Dušek, J., Eamus, D., Eichelmann, U., ElKhidir, H. A. M., Eugster, W., Ewenz, C. M., Ewers, B., Famulari, D., Fares, S., Feigenwinter, I., Feitz, A., Fensholt, R., Filippa, G., Fischer, M., Frank, J., Galvagno, M., et al.: The FLUXNET2015 dataset and the ONEFlux processing pipeline for eddy covariance data, Sci. Data, 7, 225, https://doi.org/10.1038/s41597-020-0534-3, 2020.

Peng, S.-S., Piao, S., Zeng, Z., Ciais, P., Zhou, L., Li, L. Z. X., Myneni, R. B., Yin, Y., and Zeng, H.: Afforestation in China cools local land surface temperature, Proc. Natl. Acad. Sci. U. S. A., 111, 2915–2919, https://doi.org/10.1073/pnas.1315126111, 2014.

Qu, Y., Zhu, Z., Montzka, C., Chai, L., Liu, S., Ge, Y., Liu, J., Lu, Z., He, X., Zheng, J., and Han, T.: Inter-comparison of several soil moisture downscaling methods over the Qinghai-Tibet Plateau, China, J. Hydrol., 592, 125616, https://doi.org/10.1016/j.jhydrol.2020.125616, 2021.

Radakovich, J., Houser, P., Da Silva, A., and Bosilovich, M.: Results From Global Land-surface Data Assimilation Methods, AGU Spring Meeting Abstracts, 1, 2001.

Rodell, M., Houser, P. R., Jambor, U., Gottschalck, J., Mitchell, K., Meng, C.-J., Arsenault, K., Cosgrove, B., Radakovich, J., Bosilovich, M., Entin, J. K., Walker, J. P., Lohmann, D., and Toll, D.: The Global Land Data Assimilation System, Bull. Am. Meteorol. Soc., 85, 381–394, https://doi.org/10.1175/BAMS-85-3-381, 2004.

Sandeep, P., Reddy, G. P. O., Jegankumar, R., and Kumar, K. C. A.: Monitoring of agricultural drought in semi-arid ecosystem of Peninsular India through indices derived from time-series CHIRPS and MODIS datasets, Ecol. Indic., 121, 107033, https://doi.org/10.1016/j.ecolind.2020.107033, 2021.

Shiff, S., Helman, D., and Lensky, I. M.: Worldwide continuous gap-filled MODIS land surface temperature dataset, Sci. Data, 8, 74, https://doi.org/10.1038/s41597-021-00861-7, 2021.

Sobrino, J. A., Jimenez-Munoz, J. C., and Paolini, L.: Land surface temperature retrieval from LANDSAT TM 5, Remote Sens. Environ., 90, 434–440, https://doi.org/10.1016/j.rse.2004.02.003, 2004.

Sims, D. A., Rahman, A. F., Cordova, V. D., El-Masri, B. Z., Baldocchi, D. D., Bolstad, P. V., Flanagan, L. B., Goldstein, A. H., Hollinger, D. Y., Misson, L., Monson, R. K., Oechel, W. C., Schmid, H. P., Wofsy, S. C., and Xu, L.: A new model of gross primary productivity for North American ecosystems based solely on the enhanced vegetation index and land surface temperature from MODIS, Remote Sens. Environ., 112, 1633–1646, https://doi.org/10.1016/j.rse.2007.08.004, 2008.

Toté, C., Swinnen, E., Sterckx, S., Clarijs, D., Quang, C., and Maes, R.: Evaluation of the SPOT/VEGETATION Collection 3 reprocessed dataset: Surface reflectances and NDVI, Remote Sensing of Environment, 201, 219–233, https://doi.org/10.1016/j.rse.2017.09.010, 2017.

U.S. Geological Survey: Landsat 8 Collection2 (C2) Level 2 Science Product (L2SP) Guide. Nasa, 3 (September). https://prd-wret.s3.us-west-2.amazonaws.com/assets/palladium/production/atoms/files/LSDS-1619_Landsat-8-Collection2_Level-2_Science-Product-Guide-v3.pdf., 2021.

Wan, Z.: New refinements and validation of the collection-6 MODIS land-surface temperature/emissivity product, Remote Sens. Environ., 140, 36–45, https://doi.org/10.1016/j.rse.2013.08.027, 2014.

Wang, B., Gao, P., Niu, X., and Sun, J.: Policy-driven China's Grain to Green Program: Implications for ecosystem services, Ecosyst. Serv., 27, 38–47, https://doi.org/10.1016/j.ecoser.2017.07.014, 2017.

Wang, S., Zhou, J., Lei, T., Wu, H., Zhang, X., Ma, J., and Zhong, H.: Estimating Land Surface Temperature from Satellite Passive Microwave Observations with the Traditional Neural Network, Deep Belief Network, and Convolutional Neural Network, Remote Sensing, 12, 2691, https://doi.org/10.3390/rs12172691, 2020.

Wen J., Lan Y., Su Z., Tian H., Shi X., Zhang Y., Wang X., Liu R., Zhang T., Kang Y., Lv S., and Zhang J.: Advances in observation and modeling of land surface processes over the source region of the Yellow River, Adv. Earth Sci., 26, 575–585, 2011.

Weng, Q. and Fu, P.: Modeling annual parameters of clear-sky land surface temperature variations and evaluating the impact of cloud cover using time series of Landsat TIR data, Remote Sens. Environ., 140, 267–278, https://doi.org/10.1016/j.rse.2013.09.002, 2014.

Wu, P., Shen, H., Zhang, L., and Göttsche, F.-M.: Integrated fusion of multi-scale polar-orbiting and geostationary satellite observations for the mapping of high spatial and temporal resolution land surface temperature, Remote Sens. Environ., 156, 169–181, https://doi.org/10.1016/j.rse.2014.09.013, 2015.

Xiao, Y., Zhao, W., Ma, M., Yu, W., Fan, L., Huang, Y., Sun, X., and Lang, Q.: An Integrated Method for the Generation of Spatio-Temporally Continuous LST Product With MODIS/Terra Observations, IEEE Transactions on Geoscience and Remote Sensing, 61, 1–14, https://doi.org/10.1109/TGRS.2023.3254598, 2023.

Xu, S., Cheng, J., and Zhang, Q.: A Random Forest-Based Data Fusion Method for Obtaining All-Weather Land Surface Temperature with High Spatial Resolution, Remote Sens., 13, 2211, https://doi.org/10.3390/rs13112211, 2021.

Xu, Z., Liu, S., Li, X., Shi, S., Wang, J., Zhu, Z., Xu, T., Wang, W., and Ma, M.: Intercomparison of surface energy flux measurement systems used during the HiWATER-MUSOEXE, J. Geophys. Res. Atmospheres, 118, 13,140-13,157, https://doi.org/10.1002/2013JD020260, 2013.

Yang, J. and Huang, X.: The 30 m annual land cover dataset and its dynamics in China from 1990 to 2019, Earth Syst. Sci. Data, 13, 3907–3925, https://doi.org/10.5194/essd-13-3907-2021, 2021.

Yang, J., Zhou, J., Göttsche, F.-M., Long, Z., Ma, J., and Luo, R.: Investigation and validation of algorithms for estimating land surface temperature from Sentinel-3 SLSTR data, Int. J. Appl. Earth Obs. Geoinformation, 91, 102136, https://doi.org/10.1016/j.jag.2020.102136, 2020.

Yang, N., Shi, H., Tang, H., and Yang, X.: Geographical and temporal encoding for improving the estimation of PM2.5 concentrations in China using end-to-end gradient boosting, Remote Sensing of Environment, 269, 112828, https://doi.org/10.1016/j.rse.2021.112828, 2022.

Yao, R., Wang, L., Huang, X., Cao, Q., Wei, J., He, P., Wang, S., and Wang, L.: Global seamless and high-resolution temperature dataset (GSHTD), 2001–2020, Remote Sens. Environ., 286, 113422, https://doi.org/10.1016/j.rse.2022.113422, 2023.

Yoo, C., Im, J., Cho, D., Yokoya, N., Xia, J., and Bechtel, B.: Estimation of All-Weather 1 km MODIS Land Surface Temperature for Humid Summer Days, Remote Sensing, 12, 1398, https://doi.org/10.3390/rs12091398, 2020.

Yu, G., Zhang, L., and Sun, X.: Progresses and prospects of Chinese terrestrial ecosystem flux observation and research network (ChinaFLUX), PROGRESS IN GEOGRAPHY, 33, 903–917, 2014.

Yu, P., Zhao, T., Shi, J., Ran, Y., Jia, L., Ji, D., and Xue, H.: Global spatiotemporally continuous MODIS land surface temperature dataset, Sci. Data, 9, 143, https://doi.org/10.1038/s41597-022-01214-8, 2022.

Zhai, J., Wang, L., Liu, Y., Wang, C., and Mao, X.: Assessing the effects of China's Three-North Shelter Forest Program over 40 years, Sci. Total Environ., 857, 159354, https://doi.org/10.1016/j.scitotenv.2022.159354, 2023.

Zhao, B., Mao, K., Cai, Y., Shi, J., Li, Z., Qin, Z., Meng, X., Shen, X., and Guo, Z.: A combined Terra and Aqua MODIS land surface temperature and meteorological station data product for China from 2003 to 2017, Earth Syst. Sci. Data, 12, 2555–2577, https://doi.org/10.5194/essd-12-2555-2020, 2020.

Zhan, W., Chen, Y., Zhou, J., Wang, J., Liu, W., Voogt, J., Zhu, X., Quan, J., and Li, J.: Disaggregation of remotely sensed land surface temperature: Literature survey, taxonomy, issues, and caveats, Remote Sens. Environ., 131, 119–139, https://doi.org/10.1016/j.rse.2012.12.014, 2013.

Zhao W: Daily 1km all-sky time-consistent land surface temperature dataset over the Tibetan Plateau (2001-2018), https://doi.org/10.11888/RemoteSen.tpdc.300336, 2023.

Zhang, H., Zhang, F., Zhang, G., Che, T., Yan, W., Ye, M., and Ma, N.: Ground-based evaluation of MODIS snow cover product V6 across China: Implications for the selection of NDSI threshold, Science of The Total Environment, 651, 2712–2726, https://doi.org/10.1016/j.scitotenv.2018.10.128, 2019a.

Zhang, J. and Han, S.: FLUXNET2015 CN-Cha Changbaishan, FluxNet; IAE Chinese Academy of Sciences, https://doi.org/10.18140/FLX/1440137, 2016.

Zhang, L., Jiao, W., Zhang, H., Huang, C., and Tong, Q.: Studying drought phenomena in the Continental United States in 2011 and 2012 using various drought indices, Remote Sens. Environ., 190, 96–106, https://doi.org/10.1016/j.rse.2016.12.010, 2017.

Zhang, Q. and Cheng, J.: An Empirical Algorithm for Retrieving Land Surface Temperature From AMSR-E Data Considering the Comprehensive Effects of Environmental Variables, Earth Space Sci., 7, UNSP e2019EA001006, https://doi.org/10.1029/2019EA001006, 2020b.

Zhang, Q., Wang, N., Cheng, J., and Xu, S.: A Stepwise Downscaling Method for Generating High-Resolution Land Surface Temperature From AMSR-E Data, IEEE J. Sel. Top. Appl. Earth Observ. Remote Sens., 13, 5669–5681, https://doi.org/10.1109/JSTARS.2020.3022997, 2020c.

Zhang, T., Zhou, Y., Zhu, Z., Li, X., and Asrar, G. R.: A global seamless 1 km resolution daily land surface temperature dataset (2003–2020), Earth Syst. Sci. Data, 14, 651–664, https://doi.org/10.5194/essd-14-651-2022, 2022.

Zhang, X., Zhou, J., Göttsche, F.-M., Zhan, W., Liu, S., and Cao, R.: A Method Based on Temporal Component Decomposition for Estimating 1-km All-Weather Land Surface Temperature by Merging Satellite Thermal Infrared and Passive Microwave Observations, IEEE Trans. Geosci. Remote Sens., 57, 4670–4691, https://doi.org/10.1109/TGRS.2019.2892417, 2019b.

Zhang, X., Zhou, J., Liang, S., Chai, L., Wang, D., and Liu, J.: Estimation of 1-km all-weather remotely sensed land surface temperature based on reconstructed spatial-seamless satellite passive microwave brightness temperature and thermal infrared data, ISPRS J. Photogramm. Remote Sens., 167, 321–344, https://doi.org/10.1016/j.isprsjprs.2020.07.014, 2020a.

Zhang, X., Zhou, J., Liang, S., and Wang, D.: A practical reanalysis data and thermal infrared remote sensing data merging (RTM) method for reconstruction of a 1-km all-weather land surface temperature, Remote Sens. Environ., 260, 112437, https://doi.org/10.1016/j.rse.2021.112437, 2021.

Zhang, Y.-R., Shang, G.-F., Leng, P., Ma, C., Ma, J., Zhang, X., and Li, Z.-L.: Estimation of quasi-full spatial coverage soil moisture with fine resolution in China from the combined use of ERA5-Land reanalysis and TRIMS land surface temperature product, Agric. WATER Manag., 275, https://doi.org/10.1016/j.agwat.2022.107990, 2023.

Zhao, W. and Duan, S.-B.: Reconstruction of daytime land surface temperatures under cloud-covered conditions using integrated MODIS/Terra land products and MSG geostationary satellite data, Remote Sens. Environ., 247, 111931, https://doi.org/10.1016/j.rse.2020.111931, 2020.

Zhou, S. and Cheng, J.: An Improved Temperature and Emissivity Separation Algorithm for the Advanced Himawari Imager, IEEE Trans. Geosci. Remote Sensing, 58, 7105–7124, https://doi.org/10.1109/TGRS.2020.2979846, 2020.

Zhou, J., Zhang, X., Tang, W., Ding, L., Ma, J., Zhang, X. Daily 1-km all-weather land surface temperature dataset for the Chinese landmass and its surrounding areas (TRIMS LST; 2000-2022). National Tibetan Plateau/Third Pole Environment Data Center [data set], https://doi.org/10.11888/Meteoro.tpdc.271252, 2021.

Zhou, J., Zhang, X., Zhan, W., Göttsche, F.-M., Liu, S., Olesen, F.-S., Hu, W., and Dai, F.: A Thermal Sampling Depth Correction Method for Land Surface Temperature Estimation From Satellite Passive Microwave Observation Over Barren Land, IEEE Trans. Geosci. Remote Sens., 55, 4743–4756, https://doi.org/10.1109/TGRS.2017.2698828, 2017.

Zhu, X., Duan, S.-B., Li, Z.-L., Wu, P., Wu, H., Zhao, W., and Qian, Y.: Reconstruction of land surface temperature under cloudy conditions from Landsat 8 data using annual temperature cycle model, Remote Sens. Environ., 281, 113261, https://doi.org/10.1016/j.rse.2022.113261, 2022.